

# Secure Quantum Token Processing with Color Centers in Diamond

Yannick Strocka,<sup>1</sup> Mohamed Belhassen,<sup>1</sup> Tim Schröder,<sup>1,2</sup> and Gregor Pieplow<sup>1</sup>

<sup>1</sup>*Department of Physics, Humboldt-Universität zu Berlin, 12489 Berlin, Germany*

<sup>2</sup>*Ferdinand-Braun-Institut, Leibniz-Institut für Höchstfrequenztechnik, 12489 Berlin, Germany*

We present a quantum token scheme in which the token is a quantum state that ensures secure authentication or payment. In our approach, rooted in Wiesner’s quantum money concept, a token is encoded in a multi-qubit state generated by a single-photon source and transmitted to a user who holds a quantum memory register. By leveraging state-dependent reflection from a highly efficient sawfish nanophotonic crystal cavity and implementing high-fidelity fractional quantum gates through a pulse train of optical  $\pi/8$  pulses, our design achieves gate fidelities exceeding 99% under realistic operating conditions. We also analyze microwave control, which extends the viability to longer storage times, albeit at reduced operational rates. We rigorously examine the impact of finite photon bandwidth, cavity design parameters, spectral diffusion, and control imperfections on overall performance. Our comprehensive model indicates that, with near-term improvements in device efficiency and conversion rates, the token acceptance rate can approach the MHz regime for short-distance communication links while remaining robust against optimal cloning attacks. These findings pave the way for integrating unforgeable quantum tokens into larger-scale quantum networks, thereby significantly enhancing the security of future quantum network applications.

## I. INTRODUCTION

The advent of quantum computing heralds a future in which many communication-related tasks, such as transactions [1], authentication [2], and coordination (e.g., coordinated trading) [3], could become vulnerable to attack. This potential threat has reinvigorated research into methods offering information-theoretic [4] or physical security [5] for these tasks.

Take, for example, Wiesner’s quantum money scheme [6], an idea once deemed unrealistic due to the absence of long-lived quantum memories. Although practical quantum money, which relies on very long-lived quantum memories, remains largely aspirational, shorter-lived quantum tokens – tokens that are inherently unforgeable – show promise for applications operating on shorter time scales. These applications include vendor authorization in online shopping [7] and secure user authentication in online banking, where two-factor authentication is used to verify identity through security tokens, tokenized signatures [8] for granting limited authority to autonomous systems, rapid local authentication for high-frequency trading [9], and quantum one-time memories/programs [10].

Significant advances have been achieved in purely photonic token implementations [11], including noise-tolerant approaches [12], theoretic and practical attack analyses [12–15], and s-money protocols [16]. However, to date no photonic quantum token has been stored and later retrieved from a client-held quantum memory after its generation and transmission. Quantum memories, which serve as quantum wallets, checkbooks, or credit cards, could empower clients with flexible token redemption capabilities that would otherwise necessitate much more complex schemes and coordination. Moreover, flexible token retrieval enables a single token to be exchanged among multiple clients—a capability that is not possible in schemes where the token state is irreversibly destroyed

[11, 14]. In this work, we propose a token scheme that leverages quantum memories based on negatively charged group-IV color centers in diamond (G4V) [22] integrated with high-efficiency sawfish nanophotonic crystal cavities [20, 21] to achieve reliable token storage and retrieval. G4Vs are an optimal choice for a quantum memory [23–26]. They can uniquely preserve optical coherence in diamond nanostructures due to their reduced sensitivity to charge noise [27]. Our design accommodates heterogeneous single photon sources and can compensate for their photon-to-photon frequency fluctuations (spectral diffusion [28–30]), ensuring stable performance under realistic conditions. We optimize key system aspects, including particularly cavity parameters, to enable heterogeneous integration and enhance robustness against spectral diffusion. Additionally, for token storage we introduce a novel approach for high-fidelity optical Raman spin gates using a pulse train of optical  $\pi/8$  pulses, provide closed-form expressions for an arbitrary stored photonic qubit, and derive an expression for the average token acceptance rate. Together, these contributions offer a comprehensive framework for evaluating both the performance and security of the proposed quantum token implementation.

We meticulously model the physical limitations to derive detailed design guidelines for practical implementation. In particular, we focus on the tin vacancy (SnV) [31], which offers longer coherence times [32] at a given temperature compared to the silicon vacancy (SiV) [33]. Our work examines the storage of a photonic quantum token based on Wiesner’s quantum money scheme: a simple yet robust approach that delivers well-established security bounds even under noisy conditions [34]. The token scheme further demonstrates that the proposed memories can be reliably read out, without destroying the quantum token. Notably, apart from the storage and retrieval procedure, these tokens do not require entanglement, neither between distant parties nor among the qubits that form the token state. In addition to introducing this scheme,

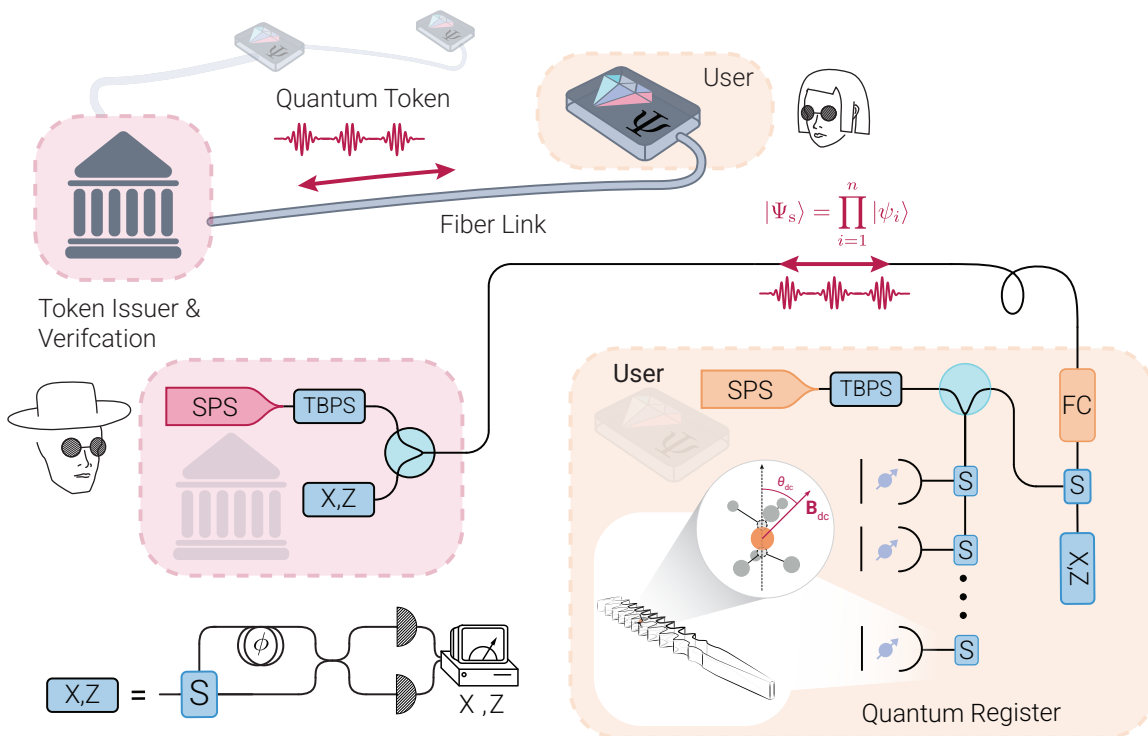


FIG. 1. In our proposed quantum token scheme enabled by G4V, the process encompasses creation, storage, retrieval, and verification. Initially, the token issuer generates a quantum token  $|\Psi_s\rangle$  along with a unique serial number  $s$ . The token is comprised of a sequence of photonic qubits  $|\psi_i\rangle$ , prepared using a single-photon source (SPS) and a time-bin qubit preparation stage (TBPS) [17–19]. This configuration allows the issuer to encode each photonic qubit in the desired quantum state. The photons are generated in the infrared spectrum so that frequency conversion (FC) is required only at the user’s end to enable interaction with the G4V. Upon transmission, the user routes and stores the token in a register composed of an array of high-efficiency sawfish [20, 21] spin-photon interfaces that host a G4V. Storage is achieved via either the electronic or nuclear spin. Fast switches (S) are deployed throughout the circuit to enable efficient measurement and routing of the token state. The  $X$ - and  $Z$ -basis measurements are performed using a fast switch integrated with an imbalanced Mach-Zehnder interferometer that features a controllable phase  $\phi$  and two detectors (shown in the lower left corner). The storage procedure is completed once the photonic qubits are sequentially measured in the  $X$ -basis. For retrieval and verification, the spin state is read out by entangling it with a photon from an SPS, which is then directed to the verifier. A subsequent  $Z$ -basis measurement on the spin is performed, and verification succeeds if the retrieved token state sufficiently matches its original preparation (see Sec. II for details).

we present a comprehensive analysis of the achievable token acceptance and redemption rates using realistic, state-of-the-art parameters, while accounting for cloning attacks [35], finite temperatures, noise and losses.

## II. TOKEN SCHEME

Fig. 1 illustrates the high-level architecture of the token scheme. The token issuer (e.g., a bank) prepares a pair of a token state and serial number  $\{|\Psi_s\rangle, s\}$ , where the token state is given by

$$|\Psi_s\rangle = \prod_{i=1}^n |\psi_i\rangle \quad (1)$$

with the number of qubits  $n$  and qubit  $|\psi_i\rangle$ , which is chosen uniformly at random from  $\{|0\rangle, |1\rangle, |+\rangle, |-\rangle\}$  ( $|\pm\rangle$

are the eigenstates of the Pauli  $\sigma_x$  matrix). The serial number  $s$  uniquely identifies the token without revealing the qubit states. We employ time-bin encoding so that

$$|\psi_i\rangle = \alpha_i |e_i\rangle + \beta_i |l_i\rangle, \quad (2)$$

where  $e_i$  and  $l_i$  denote the early and late time bins of the  $i$ -th photon. The token state  $|\Psi_s\rangle$  is generated on demand using a single photon source (SPS) [36] in conjunction with fast switches and an imbalanced Mach-Zehnder interferometer (MZI) [19, 37]. The state is then transmitted via a fiber link to the user.

At the user side, the setup comprises an SPS, an imbalanced MZI, two single photon detectors, and a quantum memory register. In its simplest form, the register consists of  $n$  sawfish cavities, each coupled to a G4V electron spin [32]. The photons are sequentially routed to the corresponding memory spins. Alternatively, an electronic spin coupled to a nuclear spin may be used [38]. Each

incoming photon becomes entangled with the electronic spin via a spin-dependent reflection [39]. The reflected photons are directed to a detector assembly featuring an imbalanced MZI and two single photon detectors. The sequence of detection events heralds the successful storage of the token state in the memory, thereby completing the token write procedure. This heralded mechanism not only ensures high fidelity in token storage but also facilitates the communication of lost qubits—an important feature for challenge-based verification schemes [11, 40].

To demonstrate the full capabilities of the spin-diamond quantum memory register, the user can send the token back to the issuing entity for verification, as required in Wiesner’s original scheme. This read-out process is achieved via a local SPS, an additional reflection-based spin-photon entanglement gate, and a subsequent spin projection measurement. When the issuer acts as the sole verifier, verification is performed by measuring the photons of the token state  $|\Psi_s\rangle$  in a basis determined by the serial number  $s$  and comparing the outcomes with the tabulated expected results. Verification succeeds when a sufficient number of qubits match the expected values.

### III. TOKEN CREATION, STORAGE AND RETRIEVAL

The success of token verification depends on its creation, storage, retrieval, and verification. This section outlines the key assumptions and steps of the protocol.

#### A. Token Creation

We assume an on-demand SPS, such as a quantum dot [41], color center [42], or atom [43]. Either the SPS operates directly in the telecom C-band, which minimizes transmission losses and eliminates the need for frequency conversion, or a frequency converter is used to shift its central frequency to the telecom C-band. In this work, we assume that the emitter operates in the telecom C-band and that the photons can be converted to the optical range at the user’s end. We require that the user can adjust the photons’ central frequency  $\omega_0$  to optimize the storage process.

The SPS photons have finite bandwidth (Fig. 2a), and a time-bin qubit preparation stage (TBPS) [17, 18] converts them at random into  $|e_i, l_i\rangle$  or  $|\pm_i\rangle = (|e_i\rangle \pm |l_i\rangle)/\sqrt{2}$ . The rapid phase modulation required to enable such swift changes is an active area of research [19]. The corresponding phase settings are recorded and linked to a unique serial number  $s$ .

We account for photon-to-photon fluctuations (spectral diffusion) but neglect multiphoton contributions, as weak coherent pulses and quantum dot double excitations have minimal impact. Notably, some closely related token schemes remain secure against multi-photon attacks

[11].

#### B. Token Storage and Retrieval

Token storage relies on a phase gate between individual spins and photons using a spin-dependent reflection scheme at the sawfish cavity interface [39], followed by a projective measurement that heralds the stored state (Fig. 2). The detailed procedure is provided in App. B.

For the idealized single-photon case in the optical range, we outline the required control sequence and the necessity of bandwidth matching for finite-bandwidth photons. The reflection coefficient for an incident mode with frequency  $\omega$  is given by [44]

$$r(\omega) = -1 + \frac{2\kappa_l(-i\Delta_a + \Gamma)}{(-i\Delta_c + \kappa)(-i\Delta_a + \Gamma) + |g|^2} \quad (3)$$

$$= |r(\omega)|e^{i\phi(\omega)} \quad (4)$$

where  $\Delta_a = \omega - \omega_a$ ,  $\Delta_c = \omega - \omega_c$ , and  $\omega_c = \omega_a - \delta$ . Here,  $\omega_a$  is the energy splitting between levels  $|A\rangle$  and  $|1\rangle$  [33],  $\omega_c$  is the cavity resonance frequency,  $\kappa$  is the cavity linewidth (FWHM),  $g$  is the coupling strength, and  $\Gamma$  is the relaxation rate from  $|A\rangle$  to  $|1\rangle$  as illustrated in Fig. 2.

We assume a half-open cavity with negligible internal losses, which we incorporate into the cavity-to-fiber coupling efficiency [20]. The cavity mode is considered to couple only  $|1\rangle$  and  $|A\rangle$ .

We define the state-dependent reflection coefficients as

$$r_1(\omega) = r(\omega) = |r_1(\omega)|e^{i\phi_1(\omega)} \quad (5)$$

$$r_2(\omega) = r(\omega - \omega_s) = |r_2(\omega)|e^{i\phi_2(\omega)}, \quad (6)$$

where  $\omega_s$  is the spin splitting.

As shown in Fig. 2, after initializing the spin in  $|1\rangle$ , an incident photon  $\alpha|e\rangle + \beta|l\rangle$  interacts with the spin via state-dependent reflection, separated by a  $\pi/2$  rotation between time bins. Ideally, the reflection phase is perfectly correlated with the spin state, leading to transformations such as  $|e, l\rangle|1\rangle \rightarrow -|e, l\rangle|1\rangle$  and  $|e, l\rangle|2\rangle \rightarrow |e, l\rangle|2\rangle$ . This correlation entangles the spin and photon. A measurement of the photonic qubit in the  $X$ -basis then heralds the storage of the quantum state in the memory as  $\alpha|1\rangle \pm \beta|2\rangle$ , up to a known spin-state rotation. In the full protocol, this rotation is unnecessary if measurement outcomes are communicated to the token verifier (App. A).

The spin state can also be transferred to a nuclear spin [45], enabling longer coherence times crucial for long-distance transmissions [46] and improved token validation for extended storage durations.

State retrieval follows the same procedure: an SPS, together with a time-bin qubit preparation stage (TBPS), generates a photon in the state  $(|e\rangle + |l\rangle)/\sqrt{2}$ . This photon is reflected off the spin with another  $\pi/2$  rotation between time bins before being sent back to the issuer.

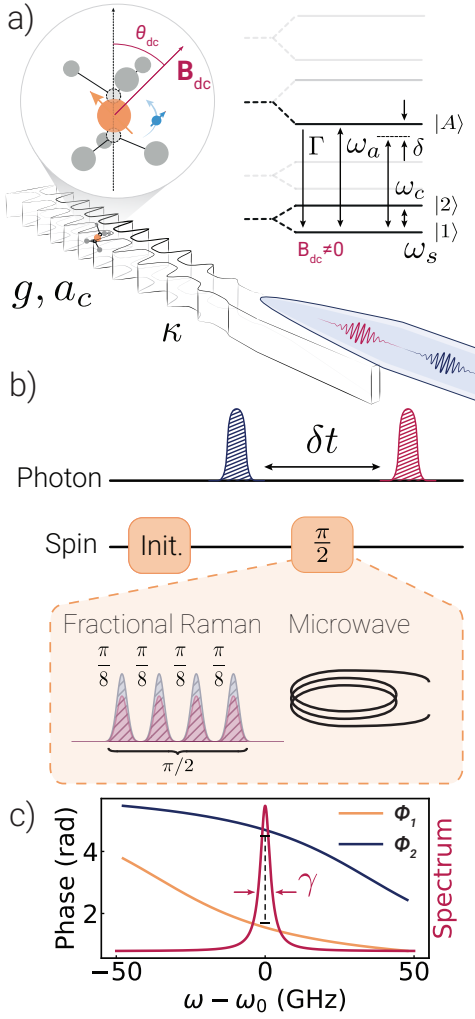


FIG. 2. a) Spin-photon entanglement is mediated via the sawfish cavity-to-fiber interface [20, 21], with the SnV center serving as a representative G4V system (electron spin in blue, nuclear spin in orange). For the reflection scheme, the SnV is modeled as a three-level system characterized by its spontaneous emission rate  $\gamma$ , spin splitting  $\omega_s$ , and an atomic transition frequency  $\omega_a$ , while interacting with a cavity mode  $a_c$  at frequency  $\omega_c$ . b) Entanglement is generated using a reflection scheme in which the spin is initially prepared in  $|1\rangle$ , and the reflection of the incoming photon is spin-dependent. A  $\pi/2$  rotation is then applied to the spin before the final reflection event. This rotation can be implemented either by a sequence of four  $\pi/8$  optical Raman pulses or via microwave control. c) The figure displays the frequency-dependent phases  $\phi_1(\omega)$  and  $\phi_2(\omega)$  [see Eqs. (5) and (6)], along with the incident photon's spectrum where  $|\phi_1(\omega) - \phi_2(\omega)| \approx \pi$ . Ideally, this phase difference remains constant across the photon's spectrum; however, variations in  $\phi_1(\omega)$  and  $\phi_2(\omega)$  across the bandwidth introduce deviations. These deviations can be minimized by optimizing the parameters  $\omega_0$ ,  $g$ ,  $\omega_c$ , and  $\kappa$  to enhance the fidelity of the spin-photon entanglement. An additional control sequence is required to transfer the spin state onto the nuclear spin for readout and storage.

A final spin measurement in the  $Z$ -basis heralds the restored photonic quantum state. Storage and retrieval measurement results are then transmitted to the verifier along with the qubit.

In an idealized scenario, incoming photons have a spectral width much narrower than the cavity response, ensuring a phase difference of  $\Delta\phi(\omega) = \phi_1(\omega) - \phi_2(\omega) = \pi$  across the photon spectrum. However, as shown in Fig. 2a, variations in  $\Delta\phi(\omega)$  due to the photon bandwidth may reduce controlled phase (CP) gate fidelities.

To mitigate these errors, the cavity response can be optimized by tuning  $g$  and  $\kappa$  [47]. This optimization is particularly important for high-rate SPSs, such as quantum dots [41], which emit broader-bandwidth photons than the cavity emitter's natural linewidth  $\Gamma$ . Furthermore, as discussed in Sec. III D, careful cavity design allows tolerance to a certain level of spectral diffusion in the SPS.

The following sections detail the optimization of the cavity design for finite-bandwidth photons, fabrication uncertainties, and coherent spin qubit control. Finally, we characterize the overall performance of the token scheme using the optimized control and cavity parameters.

### C. Coherent Control

Both reading and writing the token state make use of a  $\pi/2$  rotation around the  $y$ -axis on the Bloch sphere. This rotation can be implemented via microwave control [48–50] or through all-optical Raman control [51–54]. Each approach has distinct trade-offs. Microwave control has demonstrated high-fidelity rotations; however, it typically necessitates either a highly strained environment [48, 49] or a special magnetic field configuration [50]. Optical Raman control poses a greater challenge for achieving high-fidelity gates under low-strain conditions [54], yet it can bridge ground state splittings  $\omega_s$  that exceed the frequency range of commercially available microwave equipment. Moreover, because Raman control can handle larger ground state splittings, its quantum speed limit is substantially higher than that of microwave control—thereby enhancing transmission rates, as discussed in Sec. IV. To highlight their complementary strengths, we incorporate both control schemes in our analysis.

*Raman control:* A comprehensive explanation of an all-optical Raman control scheme is provided in [54]. In [54], we show how two laser pulses with central frequencies  $\omega_1$  and  $\omega_2$ , both detuned from the excited states, can be employed to generate high-fidelity Raman spin gates. Achieving such high fidelity requires precise tuning of several parameters: the magnetic field orientation (which lifts the spin degeneracy), the laser field strengths, the pulse duration, the relative phase, the polarization, and the detuning. As noted in [54], the primary challenge in implementing these optical spin gates is minimizing the

transient population in the excited states.

In this work we extend the findings of [54]. Instead of implementing a  $\pi/2$  gate with a single pulse, we optimize control using a pulse train in which each pulse produces a fractional rotation. As illustrated in Fig. 2b, these fractional rotations minimize transient excited-state populations compared to a single,  $\pi/2$  rotation. In our approach, a sequence of four  $\pi/8$  rotations around the  $y$ -axis of the Bloch sphere collectively yields the desired  $\pi/2$  gate. A detailed explanation of the optimization process and relevant system parameters is provided in App. B, and the optimization results are summarized in Tab. III.

We report a  $\pi/2$  gate fidelity of  $F_{\pi/2}^R = 0.9977$  for a pulse train with a total duration of  $T_g = 1.5$  ns, using an SnV center in a low-strain environment at a magnetic field of  $B_{dc} = 3.0$  T and temperature  $T = 0.1$  K. A magnetic field strength of 3.0 T was chosen because it minimizes fidelity degradation in the optical spin gates [54]. While the  $\pi/2$  gate is robust against variations in most system parameters, precise control of the magnetic field orientation and pulse phase difference is essential to maintain a fidelity above 0.9950. A detailed discussion is provided in App. C.

The reported gate fidelity accounts for both photonic and phononic relaxation, as well as phononic dephasing. The phononic contribution to the overall decoherence is calculated following the approach in [32], which explicitly includes the dependence on magnetic field orientation and strength.

*Microwave control:* In [50], it was predicted that an optimal magnetic field configuration exists for efficiently controlling the two lowest spin states of a G4V defect, regardless of strain. For our token scheme, we adopt this configuration, where the static magnetic field is oriented orthogonal to the defect's polarization axis and the microwave field is polarized along its symmetry axis. At 0.1 K,  $B_{dc} = 1.0$  T and  $B_{ac} = 1.0$  mT we obtain a microwave gate fidelity of  $F_{\pi/2}^{MW} = 0.9999$  with a gate duration of  $T_g = 34.21$  ns. Our analysis also includes the effects of phononic dephasing, which depend on the field direction.

#### D. Robust Cavity Design

We now describe how to calculate the cavity parameters  $\omega_c$ ,  $\kappa$ , and  $g$ , as well as the incident photon's central frequency  $\omega_0$ , at a given magnetic field strength  $B_{dc}$  and orientation  $\theta_{dc}$ , to maximize the controlled phase (CP) gate fidelity. We assume that  $\omega_0$  can be chosen during the frequency conversion step.

For both Raman and microwave control, the field strength and orientation are fixed. The optimal orientation is determined by the requirements of each control scheme (e.g.,  $\theta_{dc}$  in Tab. III), while the magnetic field configuration sets the relaxation and dephasing rates (see App. B 1). Both the field strength and orientation also determine the splitting between the ground and excited states.

We begin by computing the optimal cavity parameters and  $\omega_0$  from the spin-photon entanglement fidelity

$$F_{CP} = \frac{1}{16} \left| \int_{\mathbb{R}} (3r_1(\omega) - r_2(\omega)) S^2(\omega - \omega_0) d\omega \right|^2. \quad (7)$$

Here, the Lorentzian spectral function of the incident photons is given by  $S(\omega) = \gamma/2\pi [\omega^2 + (\gamma/2)^2]$ , where  $\gamma$  is the full width at half maximum (FWHM) that quantifies their bandwidth. This expression is derived in App. E based on the decomposition

$$|e, l\rangle = \int_{\mathbb{R}} S(\omega - \omega_0) |\omega\rangle_{e,l} d\omega, \quad (8)$$

with  $\langle \omega' | \omega \rangle = \delta(\omega - \omega')$  representing single-photon states in the frequency domain ( $\omega_0 \gg 0$ ). We also assume that  $g$  depends on the transition dipole strength of the  $|1\rangle \leftrightarrow |A\rangle$  transition and on  $\omega_c$  (see App. D).

Maximizing  $F_{CP}$  with respect to  $(\kappa, \omega_c, \omega_0)$  yields a set of optimal design parameters ensuring that photons with a finite bandwidth  $\gamma$  experience the desired phase shift over the relevant frequency range. However, these optimized parameters may be sensitive to fabrication uncertainties. To address this, we consider the average fidelity

$$\langle F_{CP} \rangle_S = \frac{1}{|S|} \int_S F_{CP}(\kappa + \delta\kappa, \omega_c + \delta\omega_c, \omega_0) d\delta\kappa d\delta\omega_c, \quad (9)$$

where  $S \subset \mathbb{R}^2$  is a region in the  $(\kappa, \omega_c)$  parameter space representing possible deviations. Optimizing Eq. (9) produces a cavity configuration that can be more robust against such uncertainties.

As an example, we perform this robust optimization for a quantum dot single photon source (SPS) emitting in the infrared with  $\gamma = 3.18$  GHz [55]. We assume these photons can be converted to a target optical frequency [56] and use the SnV as the representative G4V spin system. A high emission rate ensures that even if photon losses occur during transmission from the source to the quantum memory, sufficient photons still reach the memory.

We choose a magnetic field strength of  $B_{dc} = 3.0$  T and an azimuthal angle of  $\theta_{dc} = 43.11^\circ$  with respect to the defect's symmetry axis (see Tab. III). The uncertainty region is defined as  $S = \{(\delta\kappa, \delta\omega_c) \in \mathbb{R}^2 \mid -2 \text{ GHz} \leq \delta\kappa, \delta\omega_c \leq 2 \text{ GHz}\}$ , which we discretize into an equidistant grid of 25 points to reduce numerical overhead.

In Fig. 3a, we plot  $1 - F_{CP}$  over a parameter region centered in the optimized values of  $\delta = \omega_a - \omega_c$  and  $\kappa$ , as determined by optimizing Eq. (7). This optimization yields  $\kappa_{opt} = 34.07$  GHz,  $\delta_{opt} = 108.76$  GHz, and  $\omega_0 - \omega_a = -63.66$  GHz, corresponding to a cooperativity of  $C = g^2/\kappa\Gamma = 35.85$ , which is technologically feasible [23]. In this case, the minimal infidelity is  $4.90 \cdot 10^{-5}$ , and the average infidelity over  $S$  is  $1.80 \cdot 10^{-4}$ .

In Fig. 3b, we present the results from the robust optimization using Eq. (9). This yields  $\kappa_{opt} = 35.44$  GHz,  $\delta_{opt} = 99.60$  GHz, and  $\omega_0 - \omega_a = -63.66$  GHz, with

a corresponding cooperativity of  $C = 34.47$ . Here, the minimal infidelity is  $5.58 \cdot 10^{-5}$ , and the average infidelity over  $S$  is reduced to  $8.65 \cdot 10^{-5}$ .

Thus, the robust optimization improves the average infidelity by approximately a factor of two without degrading the minimal infidelity, demonstrating a clear benefit for the quantum dot - SnV system.

Overall, we conclude that high-fidelity controlled phase (CP) gates can be achieved by combining a high-bandwidth source with a G4V spin system coupled to a half-open cavity.

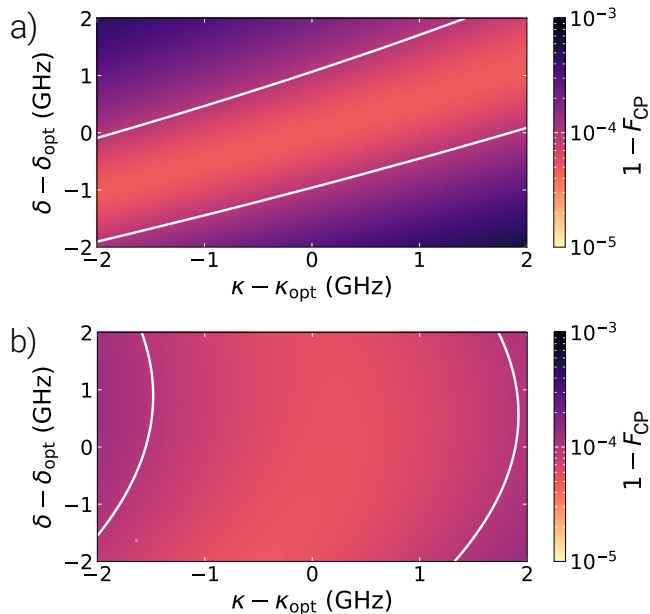


FIG. 3. Sensitivity of parameters optimized using standard and robust methods with respect to disturbances in the cavity loss rate  $\kappa$  and detuning  $\delta = \omega_a - \omega_c$ , for a SPS with a bandwidth  $\gamma = 3.18$  GHz [55] at  $B = 3.0$  T. (a) The standard optimization yields an infidelity of  $4.90 \cdot 10^{-5}$  and an average infidelity of  $1.80 \cdot 10^{-4}$  at  $\kappa_{\text{opt}} = 34.07$  GHz,  $\delta_{\text{opt}} = 108.76$  GHz,  $\omega_0 - \omega_a = -63.66$  GHz, and cooperativity  $C = 35.85$ . The contour line marks the  $10^{-4}$  infidelity threshold. (b) The robustly optimized infidelity is  $5.58 \cdot 10^{-5}$  and the average infidelity is  $8.65 \cdot 10^{-5}$ , achieved at  $\kappa_{\text{opt}} = 35.44$  GHz,  $\delta_{\text{opt}} = 99.60$  GHz,  $\omega_0 - \omega_a = -63.66$  GHz, and cooperativity  $C = 34.47$ .

#### IV. TOKEN PERFORMANCE

We now evaluate the anticipated performance of the token scheme under the optimal token storage and retrieval configuration, integrating these results with a security analysis. A system-aware security analysis is essential for fully assessing the performance of our token-memory scheme.

Analogous to the secret bit rate in communication protocols, we define an expected token acceptance rate for

a series of tokens that are issued, stored, retrieved, and returned to the verifier. This acceptance rate depends on a security parameter that sets the minimum token length required to ensure that, even in the presence of losses and noise, the probability of a successful adversarial attack is negligible [35]. In our case, the rate critically depends on transmission, conversion, and interface losses; token storage time; the type of storage spins (electronic or nuclear); the control scheme; source bandwidth; and imperfections such as spectral diffusion of the SPS that emits the token.

We consider an optimal cloning attack [35] on Wiesner's scheme as the worst-case scenario. Although perfect cloning is forbidden by the no-cloning theorem, imperfect copies of a single-qubit state can be made [13] and used to forge a token.

Let  $p_{\text{af}}$  denote the probability of successfully accepting a forged token. For an optimal cloning attack without losses, [35] gives

$$p_{\text{af}} = \alpha^n, \quad (10)$$

where  $n$  is the number of qubits in the token state and  $\alpha = 3/4$  is the single-qubit cloning probability for Wiesner's original scheme.

In the presence of losses, the probability of accepting a forged token becomes [35]

$$p_{\text{af}}(n, t) = \sum_{k=t}^n \binom{n}{k} \alpha^k (1 - \alpha)^{n-k}, \quad (11)$$

where  $t$  is the minimal number of successful measurements by the verifier out of a total of  $n$  qubits in the token.

We define a security threshold  $p_{\text{th}}$  by requiring that

$$p_{\text{af}}(t, n) < p_{\text{th}}. \quad (12)$$

This condition identifies the smallest token size  $n$  (with at least  $t < n$  successful measurements) for which the probability of accepting a fake token is below  $p_{\text{th}}$ . In our simulations, we consider thresholds of  $p_{\text{th}} = 10^{-4}$ ,  $10^{-5}$ ,  $10^{-6}$ , which can be adjusted based on the security requirements and the volume of tokens used. These thresholds will also help to illustrate how the token acceptance rate depends on the desired security level.

Tab. I lists the corresponding values for  $t$  and  $n$ , confirming that higher security demands require larger token sizes. Notably, token sizes as small as 59 qubits can reduce the probability of a forgery to one in a million. We also note that other token schemes with more relaxed bounds for  $\alpha$  [35] could further reduce the required token size. So far we have only considered the probability of accepting a forged token without accounting for the chance of a true positive verification. The probability of successfully accepting  $k$  out of  $n$  qubits in a token state is given by

$$p_a(k, \langle F \rangle) = \binom{n}{k} \langle F \rangle^k (1 - \langle F \rangle)^{n-k}. \quad (13)$$

TABLE I. Probability thresholds with corresponding token sizes

$p_{\text{th}}$	$n$	$t$
$10^{-4}$	42	41
$10^{-5}$	51	50
$10^{-6}$	59	58

The average fidelity is defined as  $\langle F \rangle = \frac{1}{4}(F_+ + F_- + F_e + F_l)$ , where  $F_x = F_x^{\text{in}} F^{\text{mem}} F_x^{\text{out}}$  for  $x = \pm, e, l$ . Here,  $F_x^{\text{in}}$  and  $F_x^{\text{out}}$  are the fidelities for the storage and retrieval processes (which include the effects of rotation gates and the finite bandwidth of the incident photons), and  $F^{\text{mem}}$  is the fidelity associated with the storage duration, which may introduce additional dephasing. This factorization is valid when individual infidelities are small [57], and for complete dephasing channels, the product provides a suitable lower bound. The detailed accounting of the error channels is provided in App. G, H.

With the true positive token verification probability, we define the average acceptance rate as

$$\gamma_a = \gamma_{\text{tok}} \sum_{k=t}^n p_a(k, \langle F \rangle) p_{\text{loss}}(n, k) \quad (14)$$

where  $\gamma_{\text{tok}}$  is the token processing rate and

$$p_{\text{loss}}(n, k) = \binom{n}{k} p_1^k (1 - p_1)^{n-k} \quad (15)$$

is the probability of losing  $k$  out of  $n$  photons during the transmission of the token. The single photon loss probability is  $p_1 = \eta_c e^{-L/L_{\text{att}}}$ , where  $\eta_c$  accounts for all the relevant interface and device efficiencies,  $L$  is the transmission fiber length and  $L_{\text{att}}$  its attenuation length. The combined interface and device efficiency is  $\eta_c = \eta_{\text{cf}}^2 \eta_{\text{fc}}^2 \eta_d^2$ .

The processing rate is defined as  $\gamma_{\text{tok}} = 1/T_n$ , assuming that the reading and writing processes require the same amount of time. The total processing time is given by

$$T_n = 2n(T_{\text{tb}} + T_g + T_m) + 2T_c + T_s, \quad (16)$$

where  $T_{\text{tb}}$  is the time allocated for a time-bin qubit,  $T_g$  is the control gate duration,  $T_m$  is the measurement time,  $T_s$  is the storage time, and  $T_c$  is the transmission time. We set  $T_{\text{tb}} = 20T_{\text{lt}}$ , where  $T_{\text{lt}}$  is the lifetime of the single photon source, and choose  $T_g = 40\sigma$  with  $\sigma = \tau_{\pi/8}/2\sqrt{2\ln(2)}$ , where  $\tau_{\pi/8}$  is the full width at half maximum of the optimized  $\pi/8$  pulse for  $B_{\text{dc}} = 3.0$  T (see Tab. III). We take  $T_m = 100$  ps [58], corresponding to the dead time of the photon detectors [59]. The communication time is given by  $T_c = L/c$ , where  $L$  is the communication distance and  $c$  is the speed of light in the fiber.

In Eq. (14), the security threshold  $p_{\text{th}}$  determines the values of  $n$  and  $t$ . Importantly, the fidelity sets the frequency of true positive events; the higher the fidelity, the higher the average acceptance rate  $\gamma_a$ .

## A. Results

The token acceptance rate  $\gamma_a$  is the key performance indicator of the scheme, allowing us to assess the diamond spin-memory register while accounting for the main error sources and an advanced attack scenario.

For our simulations, we assume a magnetic field strength of  $B_{\text{dc}} = 3.0$  T, use the  $\pi/2$  gate parameters from Tab. III, and solve the imperfect bandwidth matching problem in Eq. (7) for a given  $\gamma$  of a SPS at the optimized magnetic field orientation  $\theta_{\text{dc}}$ . The choice of  $B_{\text{dc}}$  is motivated by the relatively small cooperativity, which leads to the highest  $\pi/2$  gate fidelity for optical control (see App. F). We assume a total communication distance of  $L = 0.5$  km, extendable with quantum repeaters [60].

In Fig. 4 we study  $\gamma_a$  and its dependence on critical system parameters. Fig. 4a shows the dependence on the photon's bandwidth (assuming  $T_s = 0$  and  $\eta_c = 1$ ). Here, an increasing photon bandwidth  $\gamma = 1/(2\pi T_{\text{lt}})$  boosts the token generation rate  $1/T_n$ , but reduces the token fidelity due to imperfect bandwidth matching. The optimal bandwidth is at 5.69 GHz (corresponding to a SPS lifetime  $T_{\text{lt}} = 27.97$  ps) and yields  $\gamma_a = 80.16$  kHz for  $p_{\text{th}} = 10^{-4}$ . Such lifetimes require only moderate Purcell enhancement for quantum dots and are within reach for G4V [20].

Fig. 4b presents the token acceptance rate  $\gamma_a$  as a function of the total device efficiency  $\eta_c$  at  $\gamma_{\text{opt}}$  for each  $p_{\text{th}}$ . With current state-of-the-art values  $\eta_c \approx 0.4915$  (from  $\eta_{\text{cf}} = 0.98$ ,  $\eta_{\text{fc}} = 0.73$ , and  $\eta_d = 0.98$ ),  $\gamma_a$  is essentially zero. However, if near-future improvements bring  $\eta_c > 0.9$ , then  $\gamma_a$  starts exceeding the Hz range approaching the kHz range.

Fig. 4c shows  $\gamma_a$  as a function of the fiber length  $L$  for  $T_s = 0$  and  $\eta_c = 1$  at  $\gamma_{\text{opt}}$ , with  $\gamma_a > 10$  kHz for  $L < 1$  km for all  $p_{\text{th}}$ .

Finally, Fig. 4d depicts  $\gamma_a$  as a function of the storage time  $t$  for three scenarios: storage using the electron spin (ES) with either optical (Opt) or microwave (MW) control gates, and storage using nuclear spins (NS) (with optical control) at  $T = 0.1$  K. For microwave control [50] we assume  $B_{\text{dc}} = 1.0$  T,  $B_{\text{ac}} = 10^{-3}$  T,  $\theta_{\text{dc}} = \pi/2$ ,  $\theta_{\text{ac}} = 0$ , and  $T = 0.1$  K. Spin dephasing due to phonons is given in App. I1, and the electronic spin decay and excitation rates in App. B1. For the nuclear spin, we assume a swap fidelity of 0.9993(5) with a gate duration  $T_g = 0.1$  ms [61] and a nuclear spin dephasing time of  $T_2 = 1$  s [62] (see App. I2).

The electron spin controlled optically has an initial rate of approximately 80.16 kHz, dropping to nearly zero after about 20  $\mu\text{s}$ , while the microwave-controlled electron spin starts at around 53.22 kHz and decreases sig-

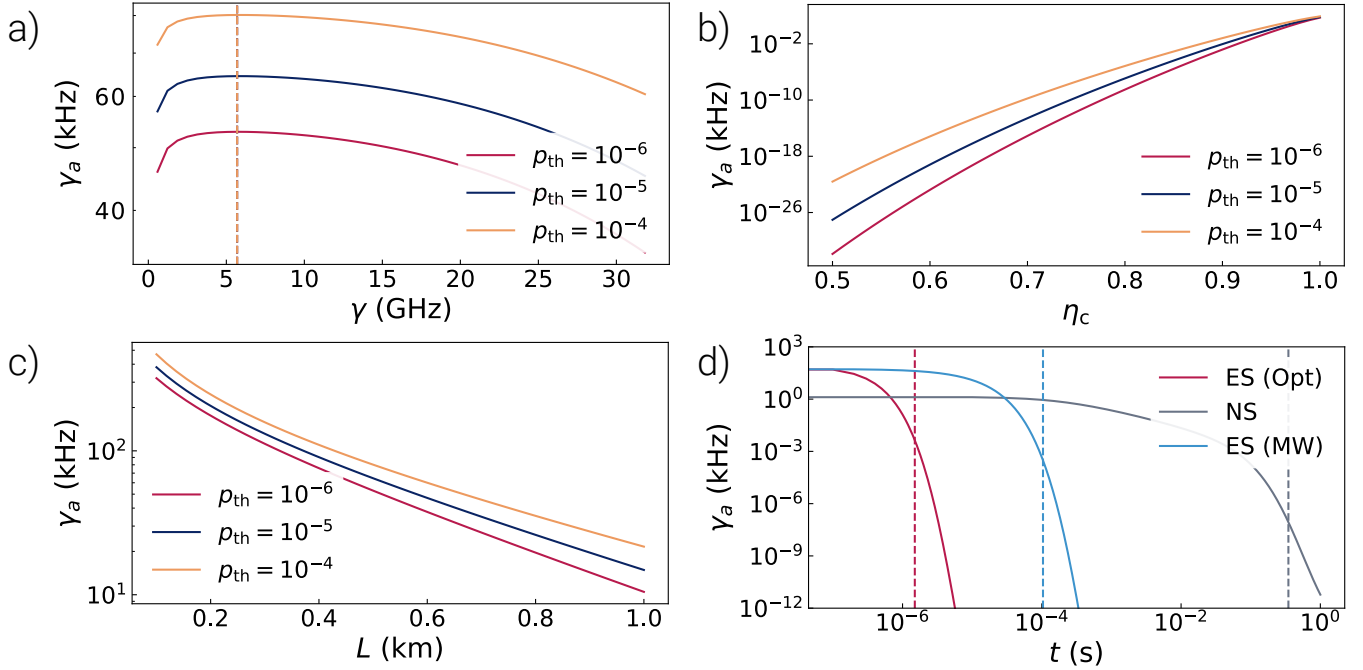


FIG. 4. Token acceptance rates under various scenarios. Unless stated otherwise, graphs a)–d) assume a fiber length of  $L = 0.5$  km, attenuation length  $L_{\text{att}} = 20$  km, operating temperature  $T = 0.1$  K, error probability threshold  $p_{\text{th}} = 10^{-4}$ , and cavity coupling efficiency  $\eta_c = 1.0$ . Storage time is zero except in d). A  $\pi/2$  gate is implemented via a pulse train of four optical  $\pi/8$  pulses. a) The acceptance rate  $\gamma_a$  is shown as a function of the incoming photon’s bandwidth  $\gamma$  for  $p_{\text{th}} = 10^{-4}, 10^{-5}, 10^{-6}$ . Dashed lines indicate the bandwidth yielding the highest acceptance; for  $p_{\text{th}} = 10^{-4}$ ,  $\gamma_{a,\text{max}} = 80.16$  kHz is achieved at  $\gamma = 5.69$  GHz. b)  $\gamma_a$  versus  $\eta_c$  is plotted at the optimal bandwidth from (a), revealing a rapid decay in rate for  $\eta_c < 0.9$ . c)  $\gamma_a$  is plotted as a function of fiber length  $L$  at the optimal  $\gamma$ , indicating that  $L$  is not the limiting factor within the considered range. d)  $\gamma_a$  is illustrated as a function of memory time  $t$  for the electron spin (ES) controlled optically (Opt) or via microwaves (MW), and for the nuclear spin (NS) at  $T = 0.1$  K. The initial rates are  $\gamma_a(0) = 80.16$  kHz for ES (Opt),  $\gamma_a(0) = 53.22$  kHz for ES (MW), and  $\gamma_a(0) = 1.36$  kHz for NS. The dashed lines denote the time  $t$  for which  $\langle F(t) \rangle$  crosses the threshold  $3/4$ .

nificantly after about 1 ms. The longer coherence time of the microwave-driven electron spin is due to a field-dependent coherence time, which is reduced for the optimal  $\theta_{\text{dc}}$  for optical control. The nuclear spin memory exhibits the longest coherence time but the lowest initial acceptance rate (1.36 kHz, exponentially decreasing after more than 10 ms).

For optical control we find a storage fidelity  $F^{\text{mem}} = 0.9895$  at the optimal  $\gamma = 5.69$  GHz, for microwave control the optimal  $\gamma = 1.22$  GHz results in  $F^{\text{mem}} = 0.9965$ , and for nuclear spin storage  $\gamma = 3.14$  GHz implies  $F^{\text{mem}} = 0.9896$ .

In summary, for short storage times the electronic spin is preferable, with optical control performing best for very short durations, while for longer storage times the nuclear spin is the better choice. Note that these results assume a worst-case attack scenario; a weaker adversary or a scheme requiring fewer photons would yield a higher  $\gamma_a$ . A challenge–response scheme [11] would already guarantee an improvement, because the token only has to be transmitted once. Finally, we examine the impact of spectral diffusion of the SPS. While spectral diffusion can limit entanglement distribution [63], since remote photons must interfere, it is less problematic here

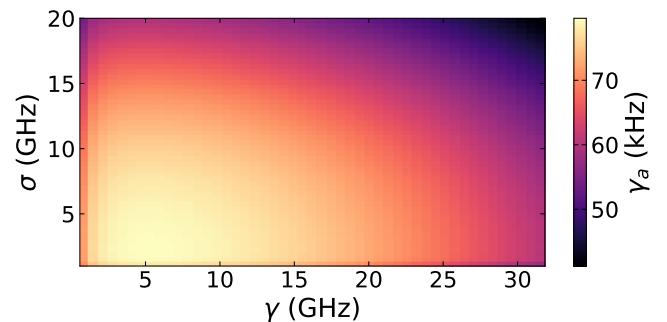


FIG. 5. Spectral diffusion’s standard deviation  $\sigma$  impact on  $\gamma_a$  for different  $\gamma$  of the incoming photons is quantified. We assume  $L = 0.5$  km,  $L_{\text{att}} = 20$  km,  $T = 0.1$  K,  $p_{\text{th}} = 10^{-4}$ ,  $\eta_c = 1$ , a pulse train of optical  $\pi/8$  pulses to achieve a  $\pi/2$  gate for  $B_{\text{dc}} = 3.0$  T (see details in Tab. III from App. B), the electron spin as the quantum memory,  $T_s = 0$  and a gaussian shape of the spectral diffusion with standard deviation  $\sigma$ .

because the incident photons only need to interfere with themselves during storage.

In Fig. 5, we show the dependence of  $\gamma_a$  on the band-

width of incoming photons and a random distribution of their central frequencies. This distribution is modeled as a normal distribution centered at  $\omega_0$  with standard deviation  $\sigma$ , in agreement with experimental observations [64] and previous theoretical studies [65]. For evaluating  $\gamma_a$  in Fig. 5 we explicitly calculate the density matrix of the stored state in the presence of spectral diffusion (see App. H).

The results indicate that  $\gamma_a$  varies only minimally across the studied parameter range, demonstrating that the acceptance rate is remarkably robust to spectral diffusion—a finding with significant implications for the tolerance of spectral diffusion in our scheme as well as for repeater applications.

## V. SUMMARY AND OUTLOOK

Our practical quantum token scheme, which leverages G4V for secure token storage and retrieval, demonstrates that classical two-factor authentication can be extended to quantum-protected and quantum-functional scenarios. By integrating robust spin-photon interfaces, high-fidelity  $\pi/2$  gates (realized via optimized pulse trains), and carefully engineered cavity parameters, we show that, even with practical constraints such as finite photon bandwidth and fabrication uncertainties, it is possible to achieve exceptional token storage and retrieval fidelities.

Our analysis indicates that with state-of-the-art device parameters and near-term improvements in conversion and coupling efficiencies, token acceptance rates can reach the kHz regime under optimal conditions. The rates shown in Fig. 4 are mainly limited by the communication distance. We estimate a processing duration of approximately 50 ns per qubit, excluding transmission time. By parallelizing the processing of individual photonic qubits through frequency and spatial multiplexing [66], and by using multiple detectors and sources on both the issuer and user sides, the acceptance rates can be drastically increased—potentially reaching the MHz regime—making the scheme highly promising for secure quantum applications.

Our performance analysis is based on detailed modeling of the G4V (specifically the SnV), including all relevant interactions and major error sources such as undesired spontaneous relaxation and phononic dephasing. By using closed analytical expressions, we efficiently perform complex parameter optimizations that yield robust optimal parameters for both the cavity and the control operations. Notably, the token acceptance rate is remark-

ably robust against spectral diffusion, since our reflection scheme accommodates wide-bandwidth photons—an advantage for both token and repeater applications.

Regarding control, we compare optical and microwave strategies and emphasize our use of fractional Raman gates to achieve the desired rotations. Although fractional gates maximize fidelity at the expense of speed, their detailed analysis is an interesting direction for future research.

Overall, these developments not only pave the way for the experimental realization of secure quantum token systems but also lay a solid foundation for integrating such protocols into larger-scale quantum networks. Future work may consider the design of a quantum register for large GHZ states [67] for enhancing security towards cloning attacks [35]. Given the proximity of the architecture to quantum repeater proposals it is straightforward to include advanced error correction techniques, that protect against photon losses [39] as well as logical errors [60].

Finally, we want to emphasize that the quantum memories are not limited to state storage; when integrated with a  $^{13}\text{C}$  spin register [68], they can also function as small quantum processors. This integration enables in-situ quantum information processing and supports advanced protocols such as quantum identification schemes based on physically unclonable functions. In this way, our proposed register not only provides robust memory capabilities but also serves as a building block for fundamentally new approaches to quantum security. Altogether, the unique properties and versatility of our design make it an exciting platform for future quantum security applications.

## ACKNOWLEDGEMENTS

Funding for this project was provided by the German Federal Ministry of Education and Research (BMBF, project QPIS, No. 16KISQ032K; project DINOQUANT 13N14921, ERC StG project QUREP of the EC, No. 851810).

## AUTHOR CONTRIBUTIONS

Y.S. and G.P. conceptualized the research, with Y.S. conducting the simulations and data analysis. M.B. performed the simulations specific to microwave spin control. G.P. and T.S. developed the core idea and provided overall project supervision. All authors contributed to writing and refining the manuscript.

---

[1] H. U. Khan, M. Sohail, S. Nazir, T. Hussain, B. Shah, and F. Ali, *J. Big Data* **10** (2023).

[2] M. A. Hassan and Z. Shukur, “A systematic review of user authentication security in electronic payment sys-

- tem,” in *Proceedings of International Conference on Data Science and Applications* (Springer Nature Singapore, 2023) p. 121–138.
- [3] M. Pinchis-Paulsen, *J. Int. Econ. Law* **25**, 527–547 (2022).
- [4] J. Shikata, *Cryptology ePrint Archive* (2015).
- [5] B. Gassend, D. Clarke, M. van Dijk, and S. Devadas, in *Proceedings of the 37th Annual IEEE/ACM International Symposium on Microarchitecture (MICRO-37)* (2004) pp. 148–160.
- [6] S. Wiesner, *ACM SIGACT News* **15**, 78 (1983).
- [7] A. Basu and S. Muylle, *Commun. of the ACM* **46**, 159–166 (2003).
- [8] S. Ben-David and O. Sattath, *Quantum* **7**, 901 (2023).
- [9] M. Karzand and L. R. Varshney, *IEEE Xplore* (2015).
- [10] A. Broadbent, S. Gharibian, and H.-S. Zhou, *Quantum* **5**, 429 (2021).
- [11] F. Pastawski, N. Y. Yao, L. Jiang, M. D. Lukin, and J. I. Cirac, *Proc. Natl. Acad. Sci. U.S.A.* **109**, 16079 (2012).
- [12] M. Georgiou and I. Kerenidis, *LIPICs, Volume 44, TQC 2015* **44**, 92 (2015).
- [13] K. Bartkiewicz, A. Černoč, G. Chimczak, K. Lemr, A. Miranowicz, and F. Nori, *npj Quantum Inf.* **3**, 1 (2017).
- [14] K. Jiráková, K. Bartkiewicz, A. Černoč, and K. Lemr, *Sci. Rep.* **9**, 16318 (2019).
- [15] A. Bilyk, J. Doliskani, and Z. Gong, *Quantum Inf. Process.* **22** (2023).
- [16] A. Kent, *Proc. R. Soc. A* **475**, 20190170 (2019).
- [17] J. P. Lee, L. M. Wells, B. Villa, S. Kalliakos, R. M. Stevenson, D. J. P. Ellis, I. Farrer, D. A. Ritchie, A. J. Bennett, and A. J. Shields, *Phys. Rev. X* **8** (2018).
- [18] F. Bouchard, D. England, P. J. Bustard, K. Heshami, and B. Sussman, *Phys. Rev. X Quantum* **3** (2022).
- [19] H. Yu, S. Sciara, M. Chemnitz, N. Montaut, B. Crockett, B. Fischer, R. Helsten, B. Wetzl, T. A. Goebel, R. G. Krämer, B. E. Little, S. T. Chu, S. Nolte, Z. Wang, J. Azaña, W. J. Munro, D. J. Moss, and R. Morandotti, *Nat. Commun.* **16** (2025).
- [20] J. M. Bopp, M. Plock, T. Turan, G. Pieplow, S. Burger, and T. Schröder, *Adv. Opt. Mater.* **12**, 2301286 (2024).
- [21] T. Pregnolato, M. E. Stucki, J. M. Bopp, M. H. V. D. Hoeven, A. Gokhale, O. Krüger, and T. Schröder, *APL Photonics* **9**, 036105 (2024).
- [22] G. Thiering and A. Gali, *Phys. Rev. X* **8**, 021063 (2018).
- [23] M. K. Bhaskar, R. Riedinger, B. Machielse, D. S. Levonian, C. T. Nguyen, E. N. Knall, H. Park, D. Englund, M. Lončar, D. D. Sukachev, and M. D. Lukin, *Nature* **580**, 60–64 (2020).
- [24] C. M. Knaut, A. Suleymanzade, Y.-C. Wei, D. R. Assumpcao, P.-J. Stas, Y. Q. Huan, B. Machielse, *et al.*, *Nature* **629**, 573 (2024).
- [25] K. C. Chen, I. Christen, H. Raniwala, M. Colangelo, L. D. Santis, K. Shtyrkova, D. Starling, R. Murphy, L. Li, K. Berggren, P. B. Dixon, M. Trusheim, and D. Englund, *Opt. Quantum* **2**, 124 (2024).
- [26] R. A. Parker, J. Arjona Martınez, K. C. Chen, A. M. Stramma, I. B. Harris, C. P. Michaels, M. E. Trusheim, M. Hayhurst Appel, C. M. Purser, W. G. Roth, D. Englund, and M. Atatüre, *Nat. Photonics* **18**, 156 (2024).
- [27] C. Bradac, W. Gao, J. Forneris, M. E. Trusheim, and I. Aharonovich, *Nat. Commun.* **10** (2019).
- [28] W. P. Ambrose and W. E. Moerner, *Nature* **349**, 225 (1991).
- [29] V. M. Acosta, C. Santori, A. Faraon, Z. Huang, K.-M. C. Fu, A. Stacey, D. A. Simpson, K. Ganesan, S. Tomljenovic-Hanic, A. D. Greentree, S. Praver, and R. G. Beausoleil, *Phys. Rev. Lett.* **108**, 206401 (2012).
- [30] L. Orphal-Kobin, K. Unterguggenberger, T. Pregnolato, N. Kemf, M. Matalla, R.-S. Unger, I. Ostermay, G. Pieplow, and T. Schröder, *Phys. Rev. X* **13**, 011042 (2023).
- [31] M. E. Trusheim, B. Pingault, N. H. Wan, M. Gündoğan, L. D. Santis, R. Debroux, D. Gangloff, C. Purser, K. C. Chen, M. Walsh, J. J. Rose, J. N. Becker, B. Lienhard, E. Bersin, I. Paradeisanos, G. Wang, D. Lyzwa, A. R.-P. Montblanch, G. Malladi, H. Bakhru, A. C. Ferrari, I. A. Walmsley, M. Atatüre, and D. Englund, *Phys. Rev. Lett.* **124** (2020).
- [32] I. B. W. Harris and D. Englund, *Phys. Rev. B* **109**, 085414 (2024).
- [33] C. Hepp, T. Müller, V. Waselowski, J. N. Becker, B. Pingault, H. Sternschulte, D. Steinmüller-Nethl, A. Gali, J. R. Maze, M. Atatüre, and C. Becher, *Phys. Rev. Lett.* **112**, 036405 (2014).
- [34] S. Wiesner, *ACM SIGACT News* **15**, 78–88 (1983).
- [35] A. Molina, T. Vidick, and J. Watrous, “Optimal counterfeiting attacks and generalizations for wiesner’s quantum money,” in *Theory of Quantum Computation, Communication, and Cryptography* (Springer Berlin Heidelberg, 2013) p. 45–64.
- [36] M. E. Reimer and C. Cher, *Nat. Photonics* **13**, 734–736 (2019).
- [37] Y. Shao, L. Chen, and S. Wen, *Microw. Opt. Technol. Lett.* **49**, 755–759 (2007).
- [38] I. B. Harris, C. P. Michaels, K. C. Chen, R. A. Parker, M. Titze, J. Arjona Martınez, M. Sutula, I. R. Christen, A. M. Stramma, W. Roth, C. M. Purser, M. H. Appel, C. Li, M. E. Trusheim, N. L. Palmer, M. L. Markham, E. S. Bielejec, M. Atatüre, and D. Englund, *Phys. Rev. X Quantum* **4** (2023).
- [39] J. Borregaard, H. Pichler, T. Schröder, M. D. Lukin, P. Lodahl, and A. S. Sørensen, *Phys. Rev. X* **10**, 021071 (2020).
- [40] M. Rozzio, A. Orioux, L. Trigo Vidarte, I. Zaquine, I. Kerenidis, and E. Diamanti, *npj Quantum Inf.* **4** (2018).
- [41] P. Senellart, G. Solomon, and A. White, *Nat. Nanotechnol.* **12**, 1026–1039 (2017).
- [42] T. Iwasaki, “Color centers based on heavy group-iv elements,” in *Diamond for Quantum Applications Part 1* (Elsevier, 2020) p. 237–256.
- [43] A. M. Basharov, *J. Exp. Theor. Phys.* **110**, 951–965 (2010).
- [44] A. Reiserer and G. Rempe, *Rev. Mod. Phys.* **87**, 1379 (2015).
- [45] H. K. C. Beukers, C. Waas, M. Pasini, H. B. van Ommen, Z. Ademi, M. Iuliano, N. Codreanu, J. M. Brevoord, T. Turan, T. H. Taminiau, and R. Hanson, *arXiv:2409.08977* (2024).
- [46] F. Wang, M. Ren, W. Sun, M. Guo, M. J. Sellars, R. L. Ahlefeldt, J. G. Bartholomew, J. Yao, S. Liu, and M. Zhong, *Phys. Rev. X Quantum* **6** (2025).
- [47] F. Omlor, B. Tissot, and G. Burkard, *Phys. Rev. A* **111** (2025).
- [48] E. I. Rosenthal, C. P. Anderson, H. C. Kleidermacher, A. J. Stein, H. Lee, J. Grzesik, G. Scuri, A. E. Rugar, D. Riedel, S. Aghaieimobodi, G. H. Ahn, K. Van Gasse,

- and J. Vučković, *Phys. Rev. X* **13**, 031022 (2023).
- [49] I. Karapatzakis, J. Resch, M. Schrodin, P. Fuchs, M. Kieschnick, J. Heupel, L. Kussi, C. Sürgers, C. Popov, J. Meijer, C. Becher, W. Wernsdorfer, and D. Hunger, *Phys. Rev. X* **14** (2024).
- [50] G. Pieplow, M. Belhassen, and T. Schröder, *Phys. Rev. B* **109**, 115409 (2024).
- [51] J. N. Becker, B. Pingault, D. Groß, M. Gündoğan, N. Kukharchyk, M. Markham, A. Edmonds, M. Atatüre, P. Bushev, and C. Becher, *Phys. Rev. Lett.* **120** (2018).
- [52] R. Debroux, C. P. Michaels, C. M. Purser, N. Wan, M. E. Trusheim, J. Arjona Martínez, R. A. Parker, A. M. Stramma, K. C. Chen, L. de Santis, E. M. Alexeev, A. C. Ferrari, D. Englund, D. A. Gangloff, and M. Atatüre, *Phys. Rev. X* **11**, 041041 (2021).
- [53] E. Takou and S. E. Economou, *Phys. Rev. B* **104** (2021).
- [54] G. Pieplow, Y. Strocka, M. Isaza-Monsalve, J. H. D. Munns, and T. Schröder, [arXiv:2312.03952](https://arxiv.org/abs/2312.03952) (2023).
- [55] P. Lodahl, A. Ludwig, and R. J. Warburton, *Phys. Today* **75**, 44–50 (2022).
- [56] S. Zaske, A. Lenhard, C. A. Kessler, C. Hepp, W. H. R. Koslowski, and M. Becher, *Opt. Express* **19**, 12825 (2011).
- [57] A. Gilchrist, N. K. Langford, and M. A. Nielsen, *Phys. Rev. A* **71**, 062310 (2005).
- [58] S. Cherednichenko, N. Acharya, E. Novoselov, and V. Drakinskiy, *Supercond. Sci. Technol.* **34**, 044001 (2021).
- [59] S. Grotowski, L. Zugliani, B. Jonas, R. Flaschmann, C. Schmid, S. Strothauer, F. Wietschorke, N. Bruckmoser, M. Müller, M. Althammer, R. Gross, K. Müller, and J. Finley, *Sci. Rep.* **15** (2025).
- [60] K. J. Wo, G. Avis, F. Rozpedek, M. F. Mor-Ruiz, G. Pieplow, T. Schröder, L. Jiang, A. S. Sørensen, and J. Borregaard, *npj Quantum Inf.* **9** (2023).
- [61] H. P. Bartling, J. Yun, K. N. Schymik, M. van Riggen, L. A. Enthoven, H. B. van Ommen, M. Babaie, F. Sebastiano, M. Markham, D. J. Twitchen, and T. H. Taminiau, [arXiv:2403.10633](https://arxiv.org/abs/2403.10633) (2024).
- [62] N. Grimm, K. Senkalla, P. J. Vetter, J. Frey, P. Gundlapalli, T. Calarco, G. Genov, M. M. Müller, and F. Jelezko, *Phys. Rev. Lett.* **134**, 043603 (2025).
- [63] S. D. Barrett and P. Kok, *Phys. Rev. A* **71**, 060310 (2005).
- [64] L. Orphal-Kobin, C. G. Torun, J. M. Bopp, G. Pieplow, and T. Schröder, *Adv. Quantum Technol.* (2024).
- [65] B. Kambs and C. Becher, *New J. Phys.* **20**, 115003 (2018).
- [66] L. Komza, X. Zhang, H. Song, Y.-L. Tang, X. Wei, and A. Sipahigil, [arXiv:2501.17339](https://arxiv.org/abs/2501.17339) (2025).
- [67] H. Cao, L. Hansen, F. Giorgino, L. Carosini, P. Zahálka, F. Zilk, J. Loredó, and P. Walther, *Phys. Rev. Lett.* **132** (2024).
- [68] C. E. Bradley, J. Randall, M. H. Abobeih, R. C. Berrevoets, M. J. Degen, M. A. Bakker, M. Markham, D. J. Twitchen, and T. H. Taminiau, *Phys. Rev. X* **9** (2019).
- [69] P. Virtanen and et al., *Nat. Methods* **17**, 261–272 (2020).
- [70] D. G. Mayer, B. P. Kinghorn, and A. A. Archer, *Agric. Syst.* **83**, 315 (2005).
- [71] D. M. Olsson and L. S. Nelson, *Technometrics* **17**, 45 (1975).
- [72] M. E. Trusheim, B. Pingault, N. H. Wan, M. Gündoğan, L. De Santis, R. Debroux, D. Gangloff, C. Purser, K. C. Chen, M. Walsh, J. J. Rose, J. N. Becker, B. Lienhard, E. Bersin, I. Paradeisanos, G. Wang, D. Lyzwa, A. R.-P. Montblanch, G. Malladi, H. Bakhru, A. C. Ferrari, I. A. Walmsley, M. Atatüre, and D. Englund, *Phys. Rev. Lett.* **124**, 023602 (2020).
- [73] I. Bayn and J. Salzman, *Opt. Express* **16**, 4972 (2008).
- [74] J.-M. L. Floch, R. Bara, J. G. Hartnett, M. E. Tobar, D. Mouneyrac, D. Passerieux, D. Cros, J. Krupka, P. Goy, and S. Carroopen, *J. Appl. Phys.* **109**, 094103 (2011).
- [75] B. W. Shore and P. L. Knight, *J. Mod. Opt.* **40**, 1195 (1993).
- [76] H. J. Kimble, *Phys. Scripta* **1998**, 127 (1998).
- [77] T. T. Tran, M. Kianinia, K. Bray, S. Kim, Z.-Q. Xu, A. Gentle, B. Sontheimer, C. Bradac, and I. Aharonovich, *APL Photonics* **2**, 116103 (2017).
- [78] K. Tiurev, P. L. Mirambell, M. B. Lauritzen, M. H. Appel, A. Tiranov, P. Lodahl, and A. S. Sørensen, *Phys. Rev. A* **104**, 052604 (2021).
- [79] N. Grimm, K. Senkalla, P. J. Vetter, J. Frey, P. Gundlapalli, T. Calarco, G. Genov, M. M. Müller, and F. Jelezko, *Phys. Rev. Lett.* **134** (2025).

## Appendix A: Reading Process

The writing process consists of the first reflection, a  $\pi/2$  rotation and a second reflection [39]. The reading process works the same way. Let's assume single frequency photons, i.e.  $|e\rangle = |l\rangle = e^{i\omega_0 t}$ , a half-open cavity which yields a unity amplitude of the reflectivity and  $\phi_\downarrow(\omega_0) = \pi$ ,  $\phi_\uparrow(\omega_0) = 0$  for simplicity. The starting point is the saved spin state at the quantum memory

$$\langle +|\psi\rangle = \frac{1}{2}(-\alpha - \beta)|1\rangle + \frac{1}{2}(-\alpha + \beta)|2\rangle, \quad (\text{A1})$$

$$\langle -|\psi\rangle = \frac{1}{2}(-\alpha + \beta)|1\rangle - \frac{1}{2}(\alpha + \beta)|2\rangle. \quad (\text{A2})$$

The readout process involves an additional photon source, where the emitted photon becomes entangled with the stored spin. At the end of the process, a measurement of the spin reveals the encoded information.

Normalizing the state measured in  $|+\rangle$  is

$$|\psi_{\text{write}}\rangle = \frac{\langle +|\psi\rangle}{\mathcal{N}} = \tilde{\alpha}|1\rangle + \tilde{\beta}|2\rangle \quad (\text{A3})$$

with  $\tilde{\alpha} = \frac{1}{2\mathcal{N}}(-\alpha - \beta)$ ,  $\tilde{\beta} = \frac{1}{2\mathcal{N}}(-\alpha + \beta)$  and  $\mathcal{N} = \|\langle +|\psi\rangle\|$ . We now exemplarily perform the reading process step for the state  $|+\rangle$ . It is

$$\begin{aligned} & \frac{1}{\sqrt{2}}(|e\rangle + |l\rangle)(\tilde{\alpha}|1\rangle + \tilde{\beta}|2\rangle) \\ & \xrightarrow{\text{early reflection}} \frac{1}{\sqrt{2}}(-\tilde{\alpha}|e1\rangle + \tilde{\alpha}|l1\rangle + \tilde{\beta}|e2\rangle + \tilde{\beta}|l2\rangle) \\ & \xrightarrow{\pi/2 \text{ rotation}} \frac{1}{\sqrt{2}}\left(-\frac{\tilde{\alpha}}{\sqrt{2}}(|e1\rangle + |e2\rangle) \right. \\ & \left. + \frac{\tilde{\alpha}}{\sqrt{2}}(|l1\rangle + |l2\rangle) + \frac{\tilde{\beta}}{\sqrt{2}}(-|e1\rangle \right. \\ & \left. + |e2\rangle) + \frac{\tilde{\beta}}{\sqrt{2}}(-|l1\rangle + |l2\rangle)\right) \\ & \xrightarrow{\text{late reflection}} \frac{1}{\sqrt{2}}\left(-\frac{\tilde{\alpha}}{\sqrt{2}}(|e1\rangle + |e2\rangle) \right. \\ & \left. + \frac{\tilde{\alpha}}{\sqrt{2}}(-|l1\rangle + |l2\rangle) + \frac{\tilde{\beta}}{\sqrt{2}}(-|e1\rangle \right. \\ & \left. + |e2\rangle) + \frac{\tilde{\beta}}{\sqrt{2}}(|l1\rangle + |l2\rangle)\right). \end{aligned} \quad (\text{A4})$$

With the definitions for  $\tilde{\alpha}$  and  $\tilde{\beta}$  the state reads

$$|\psi_{\text{read}}\rangle = \frac{1}{\mathcal{N}}(\alpha|e\rangle + \beta|l\rangle)|1\rangle + \frac{1}{\mathcal{N}}(-\alpha|l\rangle + \beta|e\rangle)|2\rangle. \quad (\text{A5})$$

Measuring in the  $Z$ -basis yields the correct photonic qubit.

## Appendix B: Optimization of Optical Spin Gates

### 1. Master Equation

The time evolution of the SnV's spin qubit using a Raman scheme is governed by the Lindblad master equation

$$\dot{\rho}(t) = -i[H(t), \rho(t)] + \sum_k L_k \rho(t) L_k^\dagger - \frac{1}{2} \{L_k^\dagger L_k, \rho(t)\} \quad (\text{B1})$$

where the detailed description of the Hamiltonian  $H(t)$  and photonic decay processes using Fermi's golden rule are explained in [54]. There is new knowledge about the detailed modeling of phononic processes [32]. According to [32] the phononic decay rates for the Lindblad operators

$$L_{ij} = \sqrt{\gamma_{ij}}|j\rangle\langle i| \quad (\text{B2})$$

are

$$\gamma_{ij} = 2\pi \sum_R |h_{Rij}|^2 \chi_R |\omega_i - \omega_j|^3 n(\omega_i - \omega_j), \quad (\text{B3})$$

$$R = E_{gx}, E_{gy}, i, j = 1, 2, 3, 4 \quad (\text{B4})$$

$$\gamma_{ij} = 2\pi \sum_R |h_{Rij}|^2 \chi_R |\omega_i - \omega_j|^3 n(\omega_i - \omega_j), \quad (\text{B5})$$

$$R = E_{ux}, E_{uy}, i, j = A, B, C, D \quad (\text{B6})$$

with the coefficients

$$h_{Egx} = -S_g^\dagger(\sigma_x \otimes \mathbf{1})S_g, \quad (\text{B7})$$

$$h_{Egy} = -S_g^\dagger(\sigma_y \otimes \mathbf{1})S_g, \quad (\text{B8})$$

$$h_{Eux} = -S_u^\dagger(\sigma_x \otimes \mathbf{1})S_u, \quad (\text{B9})$$

$$h_{Euy} = -S_u^\dagger(\sigma_y \otimes \mathbf{1})S_u, \quad (\text{B10})$$

where  $S_b, b = g, u$  refers to the eigenbasis of the SnV in the ground- and excited state, respectively. The phononic absorption cross-section is given by

$$\chi_R = \sum_{m=1}^3 \int_S \frac{\hbar \text{tr}^2(D_R \mathbf{k} \mathbf{q}_{\mathbf{k}m}^T)}{16\pi^3 \rho c_{\mathbf{k}m}^5} dS. \quad (\text{B11})$$

The integration is performed over the unit sphere  $S$ , which we perform numerically. The phononic occupation number is given by

$$n(\omega) = \begin{cases} (e^{\hbar|\omega|/k_B T} - 1)^{-1}, & \omega > 0 \\ (e^{\hbar|\omega|/k_B T} - 1)^{-1} + 1, & \omega < 0 \end{cases} \quad (\text{B12})$$

where  $k_B$  is the Boltzmann constant and  $T$  the temperature.

TABLE II. Parameters for the phononic decay rates [32]

$C_{11}/\text{GPa}$	$C_{12}/\text{GPa}$	$C_{44}/\text{GPa}$	$d^g (d^u)/\text{PHz}$	$f^g (f^u)/\text{PHz}$
1079.6	126.73	578.16	0.787 (0.956)	-0.562 (-2.555)

The strain susceptibility matrices are given by [32]

$$D_{Ebx} = \begin{pmatrix} d^b & 0 & \frac{f^b}{2} \\ 0 & -d^b & 0 \\ \frac{f^b}{2} & 0 & 0 \end{pmatrix}, \quad (\text{B13})$$

$$D_{Eby} = \begin{pmatrix} 0 & -d^b & 0 \\ -d^b & 0 & \frac{f^b}{2} \\ 0 & \frac{f^b}{2} & 0 \end{pmatrix} \quad (\text{B14})$$

with  $b = g, u$ .

The velocities  $c_{\mathbf{q},m}$  are derived from the solution to the eigenvalue problem

$$\rho \omega_{\mathbf{k}m}^2 q_i = C_{ijkl} k_j k_k q_l \quad (\text{B15})$$

with Hooke's stiffness tensor  $\mathbf{C}$  for diamond, the diamond density  $\rho = 3.51 \text{ g/cm}^3$ , phononic modes  $\mathbf{q}$  and wave vector  $\mathbf{k}$ . The velocities of the phononic modes are

$$c_{\mathbf{k}m} = \frac{\omega_{\mathbf{k}m}}{k} \quad m = 1, 2, 3. \quad (\text{B16})$$

Relevant parameters for the computation of the phononic absorption cross-section are listed in Tab. II.

## 2. Optimization

We optimize for a  $\pi/2$  rotation. The operational fidelity is

$$F_d(\pi/2) = \text{tr}^2 \left( \sqrt{\sqrt{\rho_{\text{tgt}}} \rho(T) \sqrt{\rho_{\text{tgt}}}} \right) \quad (\text{B17})$$

where  $\rho_{\text{tgt}}$  is the target state and  $\rho(T)$  is the propagated state. The infidelity is defined as

$$I_d(\pi/2) = 1 - F_d(\pi/2). \quad (\text{B18})$$

The initial state is  $\rho_0 = |\psi(t_0)\rangle\langle\psi(t_0)|$  with

$$|\psi(t_0)\rangle = \frac{1}{\sqrt{2}}(|1\rangle|e\rangle + |2\rangle|l\rangle). \quad (\text{B19})$$

The target state is  $\rho_{\text{tgt}} = R_{\pi/2} \rho_0 R_{\pi/2}^\dagger$  with  $R_{\pi/2} = \frac{1}{\sqrt{2}} \begin{pmatrix} 1 & -1 \\ 1 & 1 \end{pmatrix} \otimes \mathbf{1}$ .

Throughout the optimizations we fix the magnetic field strength  $B_{\text{dc}}$  but we optimize its dc field orientation  $\theta_{\text{dc}}$ . Regarding the optical pulse we optimize

its full width at half maximum  $\tau$ , the polarization angles of the pulse 1 and 2 which are denoted as  $\phi_1, \phi_2, \theta_1, \theta_2$ , the phase between the two pulses  $\phi_p$  as well as the detuning of the pulses with respect to the lowest lying energy eigenstate in the excited state manifold  $\Delta_A$  and their amplitude  $E_1$  and  $E_2$ . Their definition is stated in [54].

We perform global optimization in Hilbert space due to numerical costs. In Hilbert space the fidelity is

$$F_f(\theta) = |\langle\psi(t_0)|U^\dagger R_\theta|\psi(t_0)\rangle|^2 \quad (\text{B20})$$

where the time evolution operator  $U$  is calculated by numerically integrating  $|\dot{\psi}\rangle = -iH(t)|\psi\rangle$  [69]. In [54] it is mentioned that the population in higher lying levels must be penalized in order to achieve high fidelity optical spin gates. To achieve this goal, we utilize two key components:

1. We introduce a penalty term

$$P_e = \frac{1}{T} \int_0^T |\psi_e(t)|^2 dt \quad (\text{B21})$$

with the gate duration  $T$  and some excited level  $e$  and

2. we apply a pulse train.

We choose a  $\pi/8$  rotation around the  $y$ -axis on the Bloch sphere as the target gate, i.e.

$$R_{\pi/8} = \cos(\pi/8)\mathbf{1} - i\sin(\pi/8)\sigma_y. \quad (\text{B22})$$

Empirically, the population in level  $e = C$  corresponding to the seventh level inside the eight-level SnV system is most influential which is the reason why we choose that level for the penalty term. The objective function is

$$J = \alpha(1 - F_f(\pi/8)) + (1 - \alpha)P_C, \quad \alpha \in [0, 1]. \quad (\text{B23})$$

To achieve high fidelity optical spin gates we apply the following procedure:

1. Minimize the objective function  $J_\alpha$  with the method differential evolution [70] for a range of values  $\alpha \in [0, 1]$ .
2. Evaluate the dissipative infidelity  $I_d(\pi/8)$  at the computed minimizer for each  $\alpha$  and choose the smallest one. The best found minimizer is called  $x_{\text{opt,de}}$ .
3. Apply Nelder-Mead's algorithm [71] on the objective function  $I_d(\pi/8)$  initializing in  $x_0 = x_{\text{opt,de}}$ . The minimizer is called  $x_{\text{opt,nm}}$ .
4. Evaluate the dissipative  $\pi/2$  gate infidelity  $I_d(\pi/2)$  in  $x_{\text{opt,nm}}$  by composing four of the optimized  $\pi/8$  gates from the previous steps.

TABLE III. Fidelities for three magnetic field strengths for the case of a pulse train of four  $\pi/8$  pulses for achieving a  $\pi/2$  gate. The pulse amplitudes are converted to an electric field strength by evaluating  $\hbar E_i/ae$  for  $i = 1, 2$  with the quantity  $a = 55$  pm [54] and the elementary charge  $e$  at the temperature  $T = 0.1$  K. A robustness analysis towards disturbances in the optimized parameters is discussed in App. C. The effective gate duration is  $T_g = 40\sigma$  with  $\sigma = \tau_{\pi/8}/(2\sqrt{2\log(2)})$  and the optimized full width half maximum  $\tau_{\pi/8}$  of the  $\pi/8$  pulse.

$B_{dc}$ (T)	$4\tau_{\pi/8}$ (ps)	$\Delta_A$ (GHz)	$\theta_{dc}$ (deg)	$\phi_1$ (deg)	$\phi_2$ (deg)	$\theta_1$ (deg)	$\theta_2$ (deg)	$\phi_p$ (deg)	$E_1$ (GHz)	$E_2$ (GHz)	$F_d(\pi/2)$
0.3	151.65	35.73	81.4	84.5	116.35	118.84	92.76	140.69	54.4	56.02	0.9942
1.0	64.23	110.53	64.62	97.66	105.31	108.93	103.88	167.31	220.44	223.05	0.9968
3.0	353.32	99.66	43.11	100.70	100.63	104.49	104.58	90.03	68.44	72.33	0.9977

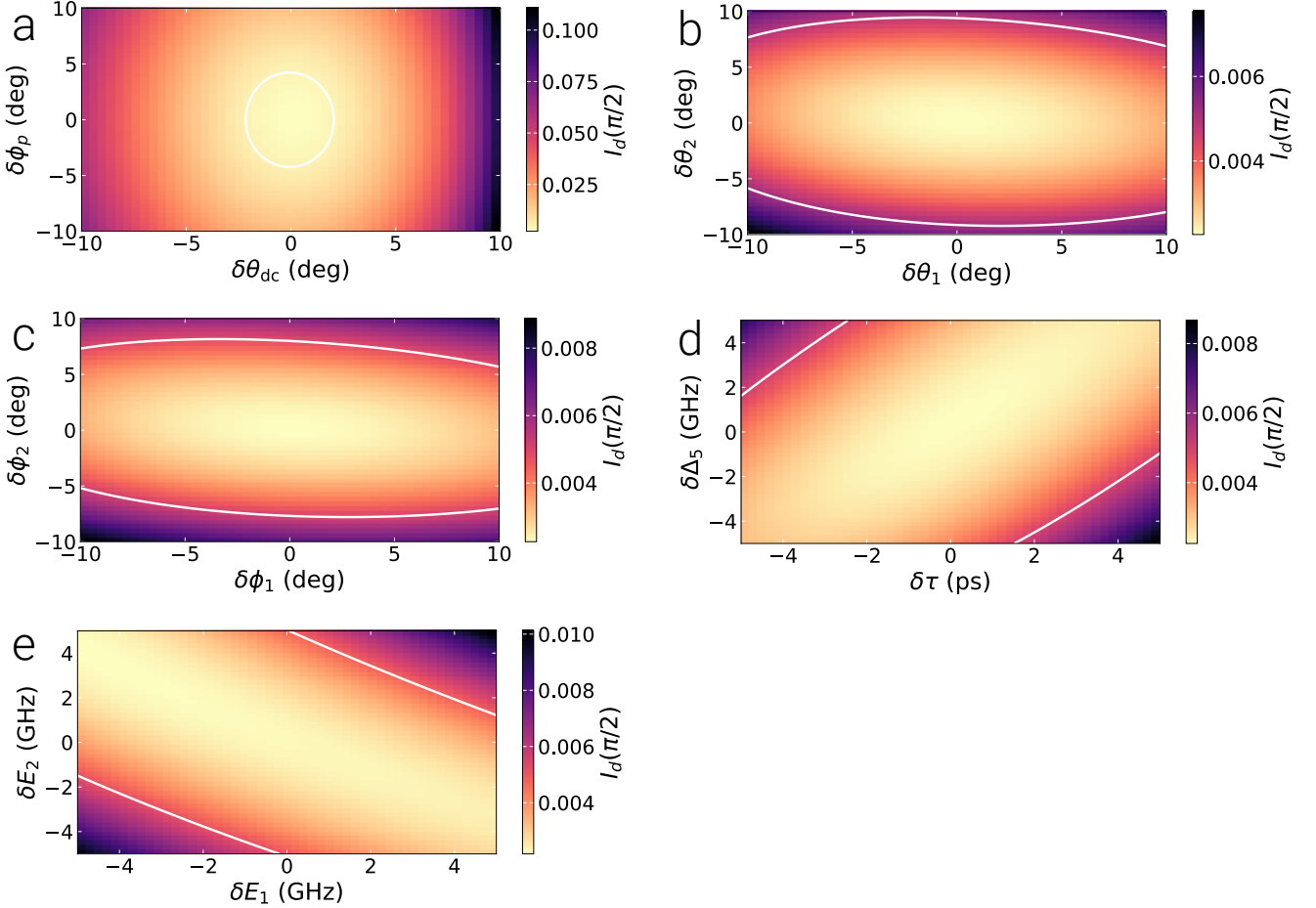


FIG. 6. Illustration of the behavior of the infidelity  $1 - F$  in a local environment around the optimized parameters  $(\phi_1, \phi_2)$  (a),  $(\phi_p, \theta_{dc})$  (b),  $(E_1, E_2)$  (c),  $(\Delta_5, \tau)$  (d) and  $(\theta_1, \theta_2)$  (e) from Tab. III for  $B_{dc} = 3.0$  T. The contour line denotes the infidelity 0.005.

Step 4 is done using linearity of the dynamical map. Consider a propagated basis state subject to a  $\pi/8$  gate  $\rho_{\pi/8}(T) = \sum_{ij} \rho_{\pi/8,ij}(T)|i\rangle\langle j|$ . To compute the propagated state under a  $\pi/2$  gate it is sufficient to apply three additional  $\pi/8$  gates, i.e.  $\rho_{\pi/2}(T) = \mathcal{D}_{\pi/8}(\mathcal{D}_{\pi/8}(\mathcal{D}_{\pi/8}(\rho_{\pi/8}(T))))$ . Using the propagated basis  $\mathcal{D}_{\pi/8}(|i\rangle\langle j|)$  for  $i, j = 1, 2$  it is straightforward to compute a propagated state under a  $\pi/2$  pulse.

In Tab. III the resulting  $\pi/2$  gate fidelities at the temperature  $T = 0.1$  K and optimized variables at the magnetic field strengths  $B_{dc} = 0.3$  T, 1.0 T, 3.0 T are listed. We find  $\pi/2$  gate fidelities exceeding 0.99 for all three magnetic field strengths which is a promising indicator for a successful use for quantum token applications.

### Appendix C: Robustness of the $\pi/2$ Gate

Since the optimized parameters from Tab. III are not exactly experimentally achievable a robustness analysis to uncertainties is provided. We analyze the behavior of the infidelity  $I_d(\pi/2)$  in a local environment of the optimized parameters. The optimized point consists of 10 components, each of which represent a physical quantity. We show five projections:

- Projection 1:  $(\theta_{dc}, \phi_p)$
- Projection 2:  $(\theta_1, \theta_2)$
- Projection 3:  $(\phi_1, \phi_2)$
- Projection 4:  $(\tau, \Delta_5)$
- Projection 5:  $(E_1, E_2)$

It is important to emphasize that these projections should not be compared against each other because the physical quantities represented by the components shown in Tab. III in each projection are fundamentally different. The visualizations attempt to show how small perturbations in specific components influence the objective function. In that way we gain a better understanding about the quantitative behavior of the infidelity in a local environment of the optimized parameters. We also want to identify a region where the infidelity stays below a certain value to provide conclusions about robustness of the  $\pi/2$  gate. We define the region of parameters

where the infidelity stays below  $5 \cdot 10^{-3}$  as the robustness region. In Fig. 6 that region lies within the contour line. We observe elliptical shapes for the robustness regions for all the projections. For all parameters except the phase  $\phi_p$  and magnetic field orientation  $\theta_{dc}$  we observe that the robustness region is almost as large as the considered area. In Fig. 6a, however, you can see that there is a sensitive dependence on the parameters  $\phi_p$  and  $\theta_{dc}$  indicating that the error of these parameters must be below approximately 3 deg for achieving an infidelity below  $5 \cdot 10^{-3}$ . The overall conclusion is that the  $\pi/2$  gate is robust to uncertainties in the pulse polarizations-, amplitudes-, length and detuning to the lowest lying energy eigenstate, however, the phase difference between the pulses and magnetic field orientation must be hit close to the optimized parameters to achieve a sufficiently low infidelity.

### Appendix D: Reflection Spectrum

In [44] the reflection spectrum of a cavity with a two-level atom is derived. Since group-IV color centers with a magnetic field are eight level systems suitable assumptions for simplifications are meritorious for modeling the reflection spectrum. The derivation is from [44].

The Hamiltonian of group-IV color centers in a diamond nanostructure with modes interacting with the color center is given by

$$H = \underbrace{\sum_{m \in G \cup E} \epsilon_m |m\rangle \langle m| + \sum_{k \in G, l \in E} \omega_{kl} a_{kl}^\dagger a_{kl} + (a_{kl} + a_{kl}^\dagger) (g_{kl} \sigma_{kl} + g_{kl}^* \sigma_{lk})}_{H_0}, \quad (D1)$$

$$g_{kl} = i \sqrt{\frac{\omega_{kl}}{2 \hbar \epsilon_0 \epsilon_r V_{kl}}} \langle k | \boldsymbol{\epsilon} \cdot \mathbf{d} | l \rangle, \quad (D2)$$

$$V_{kl} = V_{\text{eff}} \frac{\lambda_{kl}^3}{n^3} \quad (D3)$$

with  $G = \{1, 2, 3, 4\}$ ,  $E = \{A, B, C, D\}$ , the energy levels of the SnV  $\{\epsilon_m\}$  [72], the cavity mode frequencies  $\{\omega_{kl}\}$ , the creation and annihilation operators  $a_{kl}^\dagger$  and  $a_{kl}$ , the coupling coefficients  $\{g_{kl}\}$ , the dipole operator  $\mathbf{d}$ , the mode orientation  $\boldsymbol{\epsilon}$ , the mode volumes  $V_{kl}$ , the refraction index  $n$ , the wave length of the cavity mode  $\lambda_{kl} = 2\pi c/\omega_{kl}$  and the effective volume  $V_{\text{eff}} = 1.8$  for a photonic crystal cavity [73]. We choose the mode polarization in the diamond lattice basis  $\boldsymbol{\epsilon} = \mathbf{e}_z$ . In the SnV basis it is  $\mathbf{e}_z = (1/\sqrt{6}, -1/\sqrt{2}, 1/\sqrt{3})^T$ . The mode polarization vector in its most general form is constructed by rotating the  $x$  and  $y$  component of the SnV's coordinate system by an angle  $\theta$  and writing the vector  $\mathbf{e}_z$  in

that basis. That is equivalent to rotating the vector by an angle  $\theta$  around the  $z$ -axis. The map is called  $\mathbf{R}_z(\theta)$ . The result is

$$\mathbf{R}_z(\theta) \mathbf{e}_z = \begin{pmatrix} 1/\sqrt{6} \cos(\theta) + 1/\sqrt{2} \sin(\theta) \\ 1/\sqrt{6} \sin(\theta) - 1/\sqrt{2} \cos(\theta) \\ 1/\sqrt{3} \end{pmatrix}. \quad (D4)$$

In that work  $\theta = 0$  is assumed because it does not significantly influence the state fidelity. The refractive index of diamond is  $n = 2.417$  [23] and the relative susceptibility has the value  $\epsilon_r = 5.7$  [74]. It is assumed that there is only a single resonator mode which couples to

the transition from level 1 to  $A$ . The Hamiltonian yields

$$H = \underbrace{\sum_{m \in G \cup E} \epsilon_m |m\rangle \langle m| + \omega_c a_c^\dagger a_c}_{H_0} + (a_c + a_c^\dagger) (g_{1A} \sigma_{1A} + g_{1A}^* \sigma_{A1}) \quad (\text{D5})$$

with  $a_c := a_{1A}$ . Under the assumption  $\omega_c = \epsilon_A - \delta$  for some detuning  $\delta \ll \epsilon_A$  and  $\epsilon_1 = 0$  the Hamiltonian is

$$H_{\text{JC}} = H_0 + e^{-i\delta t} g_{1A} \sigma_{1A} a_c^\dagger + e^{i\delta t} g_{1A}^* \sigma_{A1} a_c \quad (\text{D6})$$

after a rotating wave approximation (RWA) which is known as the Jaynes-Cummings (JC) Hamiltonian [75]. In order to derive the reflection spectrum the Heisenberg-Langevin equations and an input-output mode relation are needed. They read [44]

$$\langle \dot{a}_c \rangle = -i \langle [a_c, H_{\text{JC}}] \rangle - \kappa \langle a_c \rangle + \sqrt{2\kappa_l} a_{\text{in},l}, \quad (\text{D7})$$

$$\langle \dot{\sigma}_{1A} \rangle = -i \langle [\sigma_{1A}, H_{\text{JC}}] \rangle - \Gamma \langle \sigma_{1A} \rangle, \quad (\text{D8})$$

$$a_{\text{out},l} + a_{\text{in},l} = \sqrt{2\kappa_l} a. \quad (\text{D9})$$

In the equation system occurs a decay rate which is computed by Fermi's golden rule. It holds [54]

$$\Gamma = \frac{4\alpha\omega_{1A}^3 n | \langle 1 | \boldsymbol{\mu} | A \rangle |^2}{3c^2 e^2} \quad (\text{D10})$$

with the fine structure constant  $\alpha = 1/137$ , the speed of light  $c$  and the elementary charge  $e$ . For the SnV it holds  $T_1 = 4.5$  ns and the Debye-Waller factor is (0.6) [54]. The transfer function from input to output mode therefore yields

$$r(\omega) = \frac{2\kappa_l (-i\Delta_a + \Gamma)}{(-i\Delta_c + \kappa)(-i\Delta_a + \Gamma) + |g_{1A}|^2} - 1 = |r(\omega)| e^{i\phi(\omega)} \quad (\text{D11})$$

with  $\Delta_a = \omega - \epsilon_A$ ,  $\Delta_c = \omega - \omega_c$  and  $\omega_c = \epsilon_A - \delta$ . We assume a half-open cavity. Thus, it holds  $\kappa_l = \kappa$ . The cooperativity is [76]

$$C = \frac{|g_{1A}|^2}{\kappa\Gamma}. \quad (\text{D12})$$

The reflection depends on the atomic state. If it is in the lowest energy eigenstate  $|1\rangle$  the reflection is given by  $r_1(\omega) = r(\omega)$ . In  $|2\rangle$  the frequencies are shifted by the spin splitting, i.e.  $r_2(\omega) = r_1(\omega - \omega_s)$ .

## Appendix E: Reflection Scheme with Imperfect Bandwidth Matching

It is assumed that there is a half-open cavity, i.e.  $\kappa_l = \kappa$ . Furthermore the incoming photon in the early and late bin have the spectrum  $S$  with central frequency  $\omega_0$ . The spectrum is assumed to be lorentzian [77]

$$S(\omega) = \mathcal{N} \tilde{S}(\omega) \quad (\text{E1})$$

with

$$\tilde{S}(\omega) = \frac{1}{\pi} \frac{\frac{\gamma}{2}}{\omega^2 + (\frac{\gamma}{2})^2} \quad (\text{E2})$$

and  $\mathcal{N} = \left( \int_{\mathbb{R}} \tilde{S}^2(\omega) d\omega \right)^{-\frac{1}{2}}$  and the life times  $\gamma := 1/(2\pi T_{\text{lt}})$  with the life time  $T_{\text{lt}}$ . Consider the time-bin qubit basis states

$$|e\rangle = \int_{\mathbb{R}} S(\omega - \omega_0) |\omega\rangle_e d\omega, \quad (\text{E3})$$

$$|l\rangle = \int_{\mathbb{R}} S(\omega - \omega_0) |\omega\rangle_l d\omega. \quad (\text{E4})$$

The photonic qubit consequently reads

$$|\psi_{\text{ph}}\rangle = \alpha |e\rangle + \beta |l\rangle = \int_{\mathbb{R}} S(\omega - \omega_0) (\alpha |\omega\rangle_e + \beta |\omega\rangle_l) d\omega. \quad (\text{E5})$$

Only the phase of the reflection spectrum matters here since transmitted light gets reflected almost perfectly due to the half-open cavity. However, the small losses due to the decay of the atom can still cause imperfect reflection. Therefore, it is still taken into account for the fidelity. Let  $r_1$  and  $r_2$  be the complex reflection coefficients. The scheme which encounters an arbitrary bandwidth of the incoming photons is as follows:

$$\begin{aligned}
|\psi_{\text{ph}}\rangle|1\rangle &= \int_{\mathbb{R}} S(\omega - \omega_0) (\alpha|\omega\rangle_e|1\rangle + \beta|\omega\rangle_l|1\rangle) d\omega \\
\text{early reflection} \xrightarrow{\quad} & \int_{\mathbb{R}} S(\omega - \omega_0) (r_1(\omega)\alpha|\omega\rangle_e|1\rangle + \beta|\omega\rangle_l|1\rangle) d\omega \\
\pi/2 \text{ rotation} \xrightarrow{\quad} & \int_{\mathbb{R}} S(\omega - \omega_0) \left( r_1(\omega) \frac{\alpha}{\sqrt{2}} |\omega\rangle_e (|1\rangle + |2\rangle) + \frac{\beta}{\sqrt{2}} |\omega\rangle_l (|1\rangle + |2\rangle) \right) d\omega \\
\text{late reflection} \xrightarrow{\quad} & \int_{\mathbb{R}} S(\omega - \omega_0) \left( r_1(\omega) \frac{\alpha}{\sqrt{2}} |\omega\rangle_e (|1\rangle + |2\rangle) \right. \\
& \left. + \frac{\beta}{\sqrt{2}} |\omega\rangle_l (r_1(\omega)|1\rangle + r_2(\omega)|2\rangle) \right) d\omega \\
(\pi/2 \text{ rotation}) \xrightarrow{\quad} & \int_{\mathbb{R}} S(\omega - \omega_0) \left( r_1(\omega)\alpha|2\rangle|\omega\rangle_e \right. \\
& \left. + \frac{\beta}{2} |\omega\rangle_l (r_1(\omega) - r_2(\omega))|1\rangle + (r_1(\omega) + r_2(\omega))|2\rangle \right) d\omega = |\psi_{\text{real}}\rangle
\end{aligned} \tag{E6}$$

The fidelity is the overlap between the ideal state  $|\psi_{\text{id}}\rangle = \alpha|e2\rangle + \beta|l1\rangle$  and the state encountering the imperfect bandwidth matching  $|\psi_{\text{real}}\rangle$ . The same procedure is ap-

plied for a system of two entangled photons which are written on two cavity-spin systems. The fidelity reads then

$$F_{\text{CP}} = |\langle\psi_{\text{id}}|\psi_{\text{real}}\rangle|^2 = \left| \int_{\mathbb{R}} -r_1(\omega) S^2(\omega - \omega_0) |\alpha|^2 d\omega + \int_{\mathbb{R}} S^2(\omega - \omega_0) \frac{|\beta|^2}{2} (-r_1(\omega) + r_2(\omega)) d\omega \right|^2. \tag{E7}$$

It is sufficient to make use of  $\alpha = \beta = \frac{1}{\sqrt{2}}$ . The fidelity reads

$$F_{\text{CP}} = \frac{1}{16} \left| \int_{\mathbb{R}} (3r_1(\omega) - r_2(\omega)) S^2(\omega - \omega_0) d\omega \right|^2. \tag{E8}$$

### Appendix F: Magnetic Field Dependence of the Cooperativity

Purcell enhancement significantly influences the fidelity of the  $\pi/2$  gate. Therefore, the dependence of the cooperativity on the magnetic field is visualized when maximizing the fidelity shown in Eq. (7). In order to derive an argumentation of the resulting behavior the corresponding cavity mode detunings and loss rates are visualized as well. In Fig. 7 such an illustration is provided. In (a) we observe a decreasing cooperativity  $C$  for an increased magnetic field strength  $B_{\text{dc}}$  while the cooperativity increases for an increasing magnetic field orientation  $\theta_{\text{dc}}$ . Both properties are explained by the spin splitting. The spin splitting increases for an increasing magnetic field strength and for a decreasing field orientation. The resulting argumentation is thus simplified to the hypothesis that the cooperativity decreases for an increasing spin splitting. To provide comprehensive arguments for that statement we visualize the cavity loss rate  $\kappa$  and cavity

mode detuning  $\delta = \omega_a - \omega_c$  as a function of the magnetic field because it holds  $C = \frac{|g_{1A}|^2}{\kappa\Gamma}$  and  $|g_{1A}| \propto \sqrt{\omega_c}$ . For both quantities we observe a rise of their magnitude for an increasing spin splitting. The explanation is as follows: A large cavity loss rate, i.e. a broadband cavity leads to a broad phase spectrum. To approximately fulfill the phase condition  $\phi_1(\omega_0) - \phi_2(\omega_0) = \pi$  the spin splitting must subsequently rise. A rising detuning  $\delta$  qualitatively results in a shift of the phase spectrum which gets compensated by a rise of the spin splitting.

### Appendix G: Derivation of the Saved Spin State

The initial state of the photon is

$$|\psi_{\text{ph},0}\rangle = a|e\rangle + b|l\rangle, \quad |a|^2 + |b|^2 = 1. \tag{G1}$$

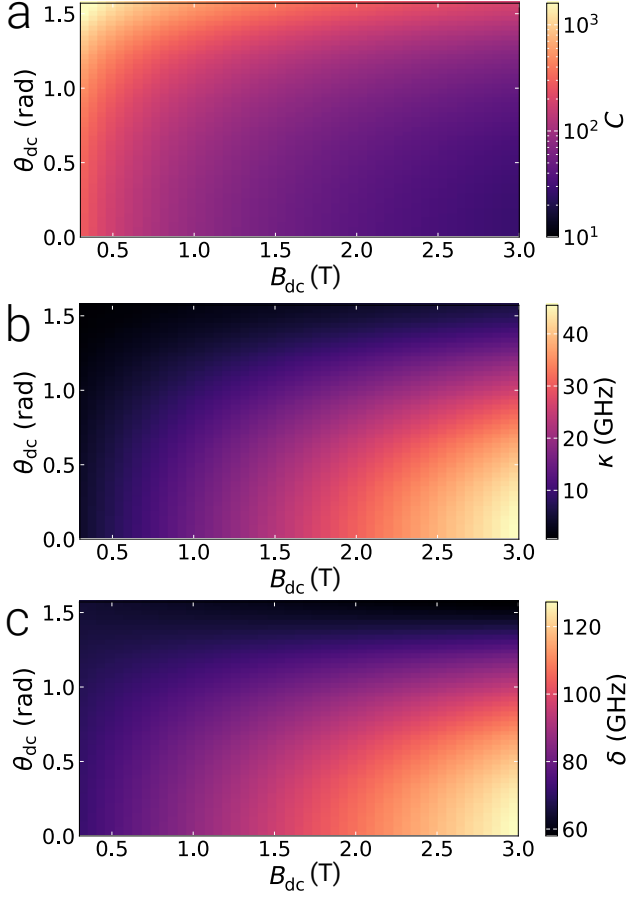


FIG. 7. Optimized cooperativity  $C$  as a function of the magnetic field orientation  $\theta_{\text{dc}}$  and strength  $B_{\text{dc}}$  for the photon bandwidth  $\gamma = 3.18$  GHz is shown. On the provided grid the fidelity is  $F_{\text{CP}} > 0.89$ .

The photon generation happens with a fidelity  $F$  [78]. This can be modeled with a depolarizing channel. It is

$$\lambda(\rho) = (1 - \epsilon)\rho + \epsilon \text{tr}(\rho) \frac{\mathbb{1}}{4}, \quad \epsilon = 2(1 - F) \quad (\text{G2})$$

where  $\rho = |\psi_{\text{ph},0}\rangle\langle\psi_{\text{ph},0}|$ . In order to model the imperfect photon bandwidth the frequency basis is used, i.e.

$$|e\rangle = \int_{\mathbb{R}} S(\omega - \omega_0) |\omega\rangle_e d\omega, \quad (\text{G3})$$

$$|l\rangle = \int_{\mathbb{R}} S(\omega - \omega_0) |\omega\rangle_l d\omega. \quad (\text{G4})$$

Subsequently, the initial state reads

$$\begin{aligned} \rho_0 &= |a|^2 |e1\rangle\langle e1| + ab^* |e1\rangle\langle l1| + a^*b |l1\rangle\langle e1| + |b|^2 |l1\rangle\langle l1| \\ &= \sum_{ij \in \mathcal{B}} \rho_{0,ij} \int_{\mathbb{R}} S(\omega - \omega_0) |\omega_{i_0} 1\rangle d\omega \int_{\mathbb{R}} S(\omega - \omega_0) \langle \omega_{j_0} 1| d\omega \end{aligned} \quad (\text{G5})$$

where  $\mathcal{B} = \{|e1\rangle, |e2\rangle, |l1\rangle, |l2\rangle\}$  and  $\rho_{0,ij} = \langle i | \rho_0 | j \rangle$  are the components of the initial state. Each step for producing spin-photon entanglement is applied modeled by the map  $\mathcal{D}$ . To keep an overview the steps are

1. Early reflection (er),
2.  $\pi/2$  rotation,

3. late reflection (lr) and
4. measurement.

We achieve to encode imperfect bandwidth matching and the imperfect  $\pi/2$  gate in the steps. The early reflection step yields the expression

$$\begin{aligned} \mathcal{D}_{\text{er}}(\rho_0) &= \sum_{ij \in \mathcal{B}} \rho_{0,ij} \int_{\mathbb{R}} S(\omega - \omega_0) (r_1(\omega) \delta_{e i_0} |\omega_{e1}\rangle + \delta_{l i_0} |\omega_{l1}\rangle) d\omega \\ &\quad \int_{\mathbb{R}} S(\omega - \omega_0) (r_1^*(\omega) \delta_{e j_0} \langle \omega_{e1}| + \delta_{l j_0} \langle \omega_{l1}|) d\omega. \end{aligned} \quad (\text{G6})$$

The imperfect  $\pi/2$  rotation is modeled by the map

$$D_{\pi/2}(|1\rangle\langle 1|) = \sum_{pq \in \{1,2\}} \Lambda_{pq} |p\rangle\langle q|. \text{ It is}$$

$$\begin{aligned} \mathcal{D}_{\pi/2}(\mathcal{D}_{\text{er}}(\rho_0)) &= \sum_{ij \in \mathcal{B}} \sum_{pq \in \{1,2\}} \rho_{0,ij} \Lambda_{pq} \int_{\mathbb{R}} S(\omega - \omega_0) (r_1(\omega) \delta_{ei_0} |\omega_e p\rangle + \delta_{li_0} |\omega_l p\rangle) d\omega \\ &\quad \int_{\mathbb{R}} S(\omega - \omega_0) (r_1^*(\omega) \delta_{ej_0} \langle \omega_e q| + \delta_{lj_0} \langle \omega_l q|) d\omega. \end{aligned} \quad (\text{G7})$$

The late reflection yields

$$\begin{aligned} \rho &= \mathcal{D}_{\text{lr}}(\mathcal{D}_{\pi/2}(\mathcal{D}_{\text{er}}(\rho_0))) = \sum_{ij \in \mathcal{B}} \sum_{pq \in \{1,2\}} \rho_{0,ij} \Lambda_{pq} \\ &\quad \int_{\mathbb{R}} S(\omega - \omega_0) (r_1(\omega) \delta_{ei_0} |\omega_e p\rangle + \delta_{p1} \delta_{li_0} r_1(\omega) |\omega_l 1\rangle + \delta_{p2} \delta_{li_0} r_2(\omega) |\omega_l 2\rangle) d\omega \\ &\quad \int_{\mathbb{R}} S(\omega - \omega_0) (r_1^*(\omega) \delta_{ej_0} \langle \omega_e q| + \delta_{q1} \delta_{lj_0} r_1^*(\omega) \langle \omega_l 1| + \delta_{q2} \delta_{lj_0} r_2^*(\omega) \langle \omega_l 2|) d\omega. \end{aligned} \quad (\text{G8})$$

After measurement in the  $X$ -basis the spin qubit reads

$$\begin{aligned} \rho_+ &= \langle + | \rho | + \rangle = \frac{1}{2} \sum_{\alpha, \beta \in \{e, l\}} \sum_{i, j \in \mathcal{B}} \sum_{p, q \in \{1, 2\}} \rho_{0,ij} \Lambda_{pq} \\ &\quad \int_{\mathbb{R}} S(\omega - \omega_0) S(\omega - \omega_0) (\delta_{\alpha e} \delta_{ei_0} r_1(\omega) |p\rangle + \delta_{\alpha l} \delta_{p1} \delta_{li_0} r_1(\omega) |1\rangle + \delta_{\alpha l} \delta_{p2} \delta_{li_0} r_2(\omega) |2\rangle) d\omega \\ &\quad \int_{\mathbb{R}} S(\omega - \omega_0) S(\omega - \omega_0) (\delta_{\beta e} \delta_{ej_0} r_1(\omega) \langle q| + \delta_{\beta l} \delta_{q1} \delta_{lj_0} r_1^*(\omega) \langle 1| + \delta_{\beta l} \delta_{q2} \delta_{lj_0} r_2^*(\omega) \langle 2|) d\omega, \end{aligned} \quad (\text{G9})$$

$$\begin{aligned} \rho_- &= \langle - | \rho | - \rangle = \frac{1}{2} \sum_{\alpha, \beta \in \{e, l\}} \sum_{i, j \in \mathcal{B}} \sum_{p, q \in \{1, 2\}} (-1)^{|\alpha|+|\beta|} \rho_{0,ij} \Lambda_{pq} \\ &\quad \int_{\mathbb{R}} S(\omega - \omega_0) S(\omega - \omega_0) (\delta_{\alpha e} \delta_{ei_0} r_1(\omega) |p\rangle + \delta_{\alpha l} \delta_{p1} \delta_{li_0} r_1(\omega) |1\rangle + \delta_{\alpha l} \delta_{p2} \delta_{li_0} r_2(\omega) |2\rangle) d\omega \\ &\quad \int_{\mathbb{R}} S(\omega - \omega_0) S(\omega - \omega_0) (\delta_{\beta e} \delta_{ej_0} r_1(\omega) \langle q| + \delta_{\beta l} \delta_{q1} \delta_{lj_0} r_1^*(\omega) \langle 1| + \delta_{\beta l} \delta_{q2} \delta_{lj_0} r_2^*(\omega) \langle 2|) d\omega. \end{aligned} \quad (\text{G10})$$

with

$$|\alpha| := \begin{cases} 0, & \text{if } \alpha = e \\ 1, & \text{else} \end{cases}, \quad |\beta| := \begin{cases} 0, & \text{if } \beta = e \\ 1, & \text{else} \end{cases} \quad (\text{G11})$$

and the  $X$ -basis of the photonic qubit

$$|+\rangle = \frac{|e\rangle + |l\rangle}{\sqrt{2}}, \quad |-\rangle = \frac{|e\rangle - |l\rangle}{\sqrt{2}}. \quad (\text{G12})$$

The state is

$$\rho = \frac{\text{tr}(\rho_{\text{tmp}})}{2} \left( \frac{\rho_+}{\text{tr}(\rho_+)} + \frac{\sigma_z \rho_- \sigma_z}{\text{tr}(\rho_-)} \right) \quad (\text{G13})$$

with

$$\rho_{\text{tmp}} = \rho_+ + \sigma_z \rho_- \sigma_z \quad (\text{G14})$$

$$\text{and } \sigma_z = \begin{pmatrix} 1 & 0 \\ 0 & -1 \end{pmatrix}.$$

## Appendix H: Spectral Diffusion of the Emitter

In a realistic setting the photon source has some spectral diffusion due to environmental charge noise. We assume a gaussian distribution of the photon's central frequency.

The distribution is

$$G(\Delta\nu) = \frac{1}{\sqrt{2\pi}\sigma} e^{-\frac{\Delta\nu^2}{2\sigma^2}} \quad (\text{H1})$$

with a standard deviation  $\sigma$  and difference between the ideal central frequency and the shifted one due to spectral diffusion  $\Delta\nu$ . In order to quantify the impact of spectral diffusion on the saved spin state a convolution of the state  $\rho(\omega_0)$  and the gaussian distribution  $G(\omega_0)$  is evaluated. The states are

$$\begin{aligned} \bar{\rho}_+ &= \langle +|\bar{\rho}|+ \rangle = \frac{1}{2} \sum_{\alpha, \beta \in \{e, l\}} \sum_{i, j \in \mathcal{B}} \sum_{p, q \in \{1, 2\}} \rho_{0, ij} \Lambda_{pq} \\ &\iint_{\mathbb{R}^2} G(\nu - \omega_0) S(\omega - \nu) S(\omega - \nu) (\delta_{\alpha e} \delta_{e i_0} r_1(\omega) |p\rangle + \delta_{\alpha l} \delta_{p1} \delta_{l i_0} r_1(\omega) |1\rangle + \delta_{\alpha l} \delta_{p2} \delta_{l i_0} r_2(\omega) |2\rangle) d\omega d\nu \\ &\iint_{\mathbb{R}^2} G(\nu - \omega_0) S(\omega - \nu) S(\omega - \nu) (\delta_{\beta e} \delta_{e j_0} r_1(\omega) \langle q| + \delta_{\beta l} \delta_{q1} \delta_{l j_0} r_1^*(\omega) \langle 1| + \delta_{\beta l} \delta_{q2} \delta_{l j_0} r_2^*(\omega) \langle 2|) d\omega d\nu, \end{aligned} \quad (\text{H2})$$

$$\begin{aligned} \bar{\rho}_- &= \langle -|\bar{\rho}|- \rangle = \frac{1}{2} \sum_{\alpha, \beta \in \{e, l\}} \sum_{i, j \in \mathcal{B}} \sum_{p, q \in \{1, 2\}} (-1)^{|\alpha|+|\beta|} \rho_{0, ij} \Lambda_{pq} \\ &\iint_{\mathbb{R}^2} G(\nu - \omega_0) S(\omega - \nu) S(\omega - \nu) (\delta_{\alpha e} \delta_{e i_0} r_1(\omega) |p\rangle + \delta_{\alpha l} \delta_{p1} \delta_{l i_0} r_1(\omega) |1\rangle + \delta_{\alpha l} \delta_{p2} \delta_{l i_0} r_2(\omega) |2\rangle) d\omega d\nu \\ &\iint_{\mathbb{R}^2} G(\nu - \omega_0) S(\omega - \nu) S(\omega - \nu) (\delta_{\beta e} \delta_{e j_0} r_1(\omega) \langle q| + \delta_{\beta l} \delta_{q1} \delta_{l j_0} r_1^*(\omega) \langle 1| + \delta_{\beta l} \delta_{q2} \delta_{l j_0} r_2^*(\omega) \langle 2|) d\omega d\nu. \end{aligned} \quad (\text{H3})$$

The state is

$$\bar{\rho} = \frac{\text{tr}(\bar{\rho}_{\text{tmp}})}{2} \left( \frac{\bar{\rho}_+}{\text{tr}(\bar{\rho}_+)} + \frac{\sigma_z \bar{\rho}_- \sigma_z}{\text{tr}(\bar{\rho}_-)} \right) \quad (\text{H4})$$

with

$$\bar{\rho}_{\text{tmp}} = \bar{\rho}_+ + \sigma_z \bar{\rho}_- \sigma_z. \quad (\text{H5})$$

## Appendix I: Decoherence of the Saved State

### 1. Electronic Spin

When the state is saved in the quantum memory there is dephasing. We model this with a two-level system governed by the Lindblad master equation in the rotating frame

$$\dot{\rho} = \sum_{k=1}^2 L_k \rho L_k^\dagger - \frac{1}{2} \{L_k^\dagger L_k, \rho\}, \quad (\text{I1})$$

$$\rho(0) = \rho_0 \quad (\text{I2})$$

with the Lindblad operators

$$L_1 = \sqrt{\gamma_-} \sigma_-, \quad L_2 = \sqrt{\gamma_+} \sigma_+ \quad (\text{I3})$$

where  $\sigma_-$  and  $\sigma_+$  describe the rising and lowering operator respectively and the initial state

$$\rho_0 = \begin{pmatrix} \rho_{00} & \rho_{01} \\ \rho_{10} & \rho_{11} \end{pmatrix} \quad (\text{I4})$$

which is the state saved in the color center's spin qubit derived in App. G. Solving the master equation with that initial state yields

$$\rho(t) = \begin{pmatrix} \rho_{00}(t) & \rho_{01}(t) \\ \rho_{10}(t) & \rho_{11}(t) \end{pmatrix}, \quad (\text{I5})$$

$$\rho_{00}(t) = \left( \rho_{00} - \frac{\gamma_-}{\gamma_- + \gamma_+} \right) e^{-\frac{\gamma_- + \gamma_+}{2} t} + \frac{\gamma_-}{\gamma_- + \gamma_+}, \quad (\text{I6})$$

$$\rho_{01}(t) = e^{-\frac{\gamma_- + \gamma_+}{2} t} \rho_{01}, \quad (\text{I7})$$

$$\rho_{10}(t) = e^{-\frac{\gamma_- + \gamma_+}{2} t} \rho_{10}, \quad (\text{I8})$$

$$\rho_{11}(t) = 1 - \rho_{00}(t). \quad (\text{I9})$$

### 2. Nuclear Spin

If the nuclear spin is considered to be the memory we model pure dephasing using the lindblad-operator  $L =$

$\sqrt{\gamma_d}\sigma_z$  with the dephasing rate  $\gamma_d = 1/T_d$  and  $T_d = 1$  s [79]. The propagated spin state reads

$$\rho(t) = \begin{pmatrix} \rho_{00} & \rho_{01}e^{-2\gamma_d t} \\ \rho_{10}e^{-2\gamma_d t} & \rho_{11} \end{pmatrix}. \quad (\text{I10})$$